Supplementary information for

Strongly adhesive and sustainable photopolymers via reaction-sequenced network design

Shuang-Lin Zou[1], Ying-Chun Xu[1], Jia-Hui Zhang[1], Wen-Zheng Yin[2], Qiang Wang[1], Chun-Lin Xu[3], Ling-Ping Xiao[1,4*] & Run-Cang Sun[1]

[1] Liaoning Key Lab of Lignocellulose Chemistry and BioMaterials, Liaoning Collaborative Innovation Center for Lignocellulosic Biorefinery, College of Light Industry and Chemical Engineering, Dalian Polytechnic University, Dalian 116034, China.

[2] State Key Laboratory of Bioinspired Interfacial Materials Science, Bioinspired Science Innovation center, Hangzhou International Innovation Institute, Beihang University, Hangzhou 311115, China.

[3] Laboratory of Natural Materials Technology, Faculty of Science and Engineering, Åbo Akademi University, Henrikinkatu 2, Turku FI-20500, Finland.

[4] Instrumental Analysis Center, Dalian Polytechnic University, Dalian 116034, China.

*Corresponding author. Email: lpxiao@dlpu.edu.cn (L.-P. Xiao)

The PDF file includes:

Materials and Methods
Supplementary Figs. 1 to 61
Supplementary Table 1
References

Other Supplementary Materials for this manuscript include the following:

Videos S1 to S8

Supplementary Methods

Scanning electron microscopy (SEM)

Scanning electron microscopy (SEM, JEOL JSM7800F) was used to analyze the surface morphology and acquire cross-sectional images of the photopolymers with an accelerating voltage of 10 ~ 20 kV and magnification of 5 k ~ 50 k under a N_2 atmosphere. Before the SEM study, the sample surface was sputter-coated with 2 ~ 5 nm thick gold-palladium. In addition, for cross-sectional studies, all membranes were freeze fractured in liquid nitrogen.

Contact angle measurement

To evaluate the surface wettability of the photopolymers, water contact angle measurements were conducted using a contact angle goniometer (SL 200KB K^{-1}, Kino) at room temperature. The dried photopolymer samples were affixed to a glass slide with adhesive tape, and a deionized water droplet was deposited on the membrane surface using a micro syringe. The droplet was allowed to stabilize on the sample surface, and its profile was analyzed using the 2θ fitting method. A digital camera recorded the contact angle at a rate of 3 frames per second for 30 seconds. Measurements were taken at three different locations on each sample, spaced 5 mm apart, and the average value was calculated.

X-ray photoelectron spectroscopy (XPS)

X-ray photoelectron spectroscopy (XPS) analysis was performed using a Thermon Scientific K-alpha plus spectrometer, calibrated using a C 1 s binding energy of 284.6 eV. The survey spectra and the core-level XPS spectra were recorded from at least three different spots on the samples. Data processing was performed using Thermon Advantage software (v5.992).

Differential scanning calorimetry (DSC)

The photopolymers in this study were characterized by differential scanning calorimetry (DSC) using a TA Q250 instrument. The samples were precisely weighed into aluminum crucibles and subjected to a three-stage thermal program: first heated to 150 °C at 10 °C min^{-1} followed by a 2 minutes' isothermal hold, then heated to 300 °C at the same rate, and finally cooled to 220 °C at 10 °C min^{-1}. The glass transition temperature (T_g) of each photopolymer sample was determined by analyzing the heat flow as a function of temperature during the third cooling cycle.

X-ray diffraction pattern (XRD)

X-ray diffraction (XRD) patterns were gathered over a 28 range from 10° to 80° with a 5° min^{-1} scan rate and 0.02° step size using the XRD-6100 diffractometer of Shimazu Laboratory. Only the graphs in the useful range are included in this work.

Fourier transform infrared spectroscopy (FTIR)

The FT-IR spectra of the polymer films were obtained using a PerkinElmer Frontier FT-IR spectrophotometer equipped with a diamond attenuated total reflectance (ATR) accessory. Prior to measurement, the samples were cleaned with ethanol to remove surface contaminants and dried under nitrogen flow. Spectra were collected in ATR mode with a resolution of 4 cm^{-1} over the range of 4000 ~ 650 cm^{-1}, accumulating 32 scans per measurement. The ATR crystal was carefully cleaned with isopropanol between samples to prevent cross-contamination. Real-time pressure monitoring ensured consistent sample contact with the crystal. Data were processed using Spectrum 10 software, including automatic baseline correction and atmospheric compensation.

The penetration depth was maintained at approximately 2 μm by applying constant pressure through the built-in clamp system.

Gel permeation chromatography (GPC)

The molecular weight characteristics of the photopolymers, including both the average molecular weight and polydispersity index (PDI), were determined using an Agilent 1260 Infinity gel permeation chromatography (GPC) system equipped with refractive index detection. The analysis was performed at 35 °C with tetrahydrofuran (THF) as the mobile phase at a flow rate of 1.0 mL min^{-1} through a series of PL gel mixed-B columns. A set of narrow-dispersity polystyrene standards with molecular weights ranging from 580 to 3,000,000 g mol^{-1} was employed to establish the calibration curve, which correlated elution time with molecular weight. The molecular weight parameters of the synthesized monomers were subsequently calculated by comparing their elution profiles with the established calibration curve, with all data processing performed using Agilent GPC/SEC software.

Thermal analysis (TGA)

The thermal stability of lignin samples and mass loss of epoxy polymers were determined by a Q500 thermogravimetric analyzer (TA Instruments). Approximately 10 mg sample in a small crucible were performed under a nitrogen atmosphere with temperature ranging from 25 to 600 °C at a heating rate of 10 °C min^{-1}.

Nuclear magnetic resonance (NMR) spectroscopy

The ^{1}H NMR spectra were recorded on a Bruker Ascend 400 MHz NMR spectrometer at 25 °C. Samples (10 mg) were dissolved in 0.6 mL of deuterated chloroform ($CDCl_3$). Spectra were acquired with 32 scans using a 30° pulse angle and 5 s relaxation delay.

Ultraviolet light aging test

The photopolymers were subjected to accelerated UV aging in a QUV weathering tester equipped with mercury lamps at an irradiance of 0.68 W·m^{-2}. The aging protocol consisted of alternating cycles of UV radiation at 60 °C (8 h), condensation at 80% relative humidity (4 h), and water spray (0.5 h) for a total duration of 168 h. Following this accelerated aging process, the samples were collected and their anti-aging properties were evaluated using the aforementioned characterization methods.

Transmission electron microscopy (TEM)

The microstructure of the samples was characterized by TEM using a JEM-2100(UHR) high-resolution instrument operated at 200 kV.

Dynamic thermomechanical analysis (DMA)

The dynamic thermomechanical properties were characterized using a DMA Q800 V21.2 Build 88 analyzer in tension mode. Isothermal frequency sweeps (0.1 ~ 10 Hz) were performed at 25 °C. Subsequently, dynamic temperature scans (0 ~ 150 °C) were conducted at 1 Hz with a heating rate of 5 °C min^{-1} under nitrogen purge. Storage modulus (E'), loss modulus (E''), and tan δ were simultaneously recorded to evaluate the viscoelastic behavior and thermal transitions of the materials.

Solvent resistance test

The adhesives prepared under various conditions were cut into sheets measuring 200 mm^2, and their initial weight was recorded. Subsequently, these samples were immersed in water for a duration of 48 h. After this period, the samples were removed from the water and their weight was measured again.

After hot pressing the adhesive material onto the bamboo sheet substrate, an equal amount of solvent was added to a beaker, and then the hot-pressed material was placed in the beaker for a few days, during which time it was sealed with a film. After a few days the adhesive was removed and placed in a ventilated area to dry, then a tensile test was performed to measure the change in properties.

Computational Modeling of Polymerization from Monomers to Networks

Calculation of the Properties of Monomer Chemical Molecules

The chemical formulae of 3,4-epoxycyclohexylmethyl-3,4-epoxycyclohexylmethacrylate, 4-acryloylmorpholine, lauryl methacrylate, diphenyl(2,4,6-trimethylbenzoyl) phosphine oxide, and cellulose molecular units were constructed using the Material Studio software. The chemical formula structures were then optimized at the GGA-BLYPD31 level in the Dmol3 functional module. The optimized chemical structure files were subsequently used to calculate the HOMO-LUMO orbital and electron cloud density distribution through the Fukui function, Orbitals, Electron density, Electrostatics, and Population analysis functional modules.

Molecular Modeling and Interaction Energy Analysis of Polymer Intermediates

The interaction energy of intermediates in the polymer compounds model was investigated. The chemical structures of 3,4-epoxycyclohexylmethyl-3,4-epoxycyclohexylformate, 4-acryloylmorpholine, lauryl methacrylate, diphenyl(2,4,6-trimethylbenzoyl) phosphine oxide (DPIPO), cellulose molecular units, and Zn^{2+} were constructed using Material Studio software. In the Forcite module, the COMPASS III force field was selected for atomic force field assignment, and subsequent molecular structure optimization and energy minimization yielded optimized molecular models. Specifically, the reaction intermediates formed by DPIPO-generated radicals adding to 3,4-epoxycyclohexylmethyl-3,4-epoxycyclohexylformate, 4-acryloylmorpholine, and lauryl methacrylate were subjected to structural and energetic optimization within the Forcite module using the COMPASS III force field. Additionally, the molecular models resulting from the condensation reactions of cellulose molecular units and the complexation with Zn^{2+} were also optimized for structure and energy using the same protocol.

Polymer compounds model

The amorphous cell module was utilized to calculate the polymer compounds model. The chemical structures of 3,4-epoxycyclohexylmethyl-3,4-epoxycyclohexylformate, 4-acryloylmorpholine, lauryl methacrylate, diphenyl(2,4,6-trimethylbenzoyl) phosphine oxide (DPIPO), and cellulose molecular units were constructed using Material Studio software. In the Forcite module, the COMPASS III force field was selected for atomic force field assignment, and subsequent molecular structure optimization and energy minimization yielded optimized molecular models. Based on the monomer proportions described in the Preparation methods section, the polymer molecular model was constructed using the Amorphous Cell module with the COMPASS III force field, and a 50 ns simulation was set up.

Life Cycle Assessment (LCA)

In accordance with the ISO 14040 series, the LCA was conducted in four distinct phases: goal and scope definition, life cycle inventory (LCI), life cycle impact assessment (LCIA), and interpretation of results. The objective of this study is to quantify the environmental impact of the adhesives produced in this experiment and to compare them with EVA adhesives derived from fossil sources. The functional unit is defined as 1 kg of both EAL30/Zn and EVA adhesives. The system boundary encompasses the entire life cycle "from cradle to gate". The life cycle list of EAL30/Zn is based on the experimental ratio and the energy consumption of the process. For fossil-derived EVA, the data comes from the current raw material data of EVA resin. The background data is from the Ecoinvent®v3.3 database embedded in SimaPro software. A life cycle list of 1 Kg products was established based on the production process.

The ReCiPe2016 (H) method was employed for impact assessment, evaluating 18 environmental impact categories. These categories include global warming potential (GWP, kg CO_2 eq.), stratospheric ozone depletion (ODP, kg CFC11 eq.), ionizing radiation (IRP, kBq Co-60 eq.), ozone formation-human health (HOFP, kg NOx eq.), fine particulate matter formation (PMFP, kg PM 2.5 eq.), ozone formation-terrestrial ecosystems (EOFP, kg NOx eq.), terrestrial acidification (TAP, kg SO_2 eq.), freshwater eutrophication (FEP, kg P eq.), marine eutrophication (MEP, kg N eq.), terrestrial ecotoxicity (TETP, kg 1,4-DCB), freshwater ecotoxicity (FETP, kg 1,4-DCB), marine ecotoxicity (METP, kg 1,4-DCB), human carcinogenic toxicity (HTPc, kg 1,4-DCB), human non-carcinogenic toxicity (HTPnc, kg 1 ,4-DCB), land use impacts(LOP, m^2 a crop equivalent), mineral resource scarcity(SOP, kg Cu equivalent), fossil resource scarcity(FFP , kg oil equivalent) and water consumption(WCP, m^3).

Techno-economic analysis (TEA)

Based on the technical economic analysis (TEA) methodology employed, the cost structure for EAL variants (EAL, EAL30, EAL30/Zn) and EVA adhesives was calculated using a cradle-to-gate approach encompassing raw materials, energy consumption, equipment depreciation, environmental compliance, and packaging/transportation.

Cost analysis

Raw material cost

Raw material costs were derived from industrial-grade 2024 market prices, incorporating a 5% loss-adjusted mass ratio for each component, while energy costs were computed based on specific equipment power ratings (e.g., 5 Kw mixer, 10 kW UV system), operational durations per unit output, China's industrial electricity rate ($0.12 kWh^{-1}), and an 80% energy utilization efficiency. The basis for price calculation: The median of the industrial-grade price range for the pilot scale (50 tons year^{-1}) is selected at $8.5 kg^{-1}, which conforms to the cost assumption of commercial production. The cost structure integrates raw material costs, synthesis processes, purification, transportation and storage.

$$\mathrm{Cost}_{\mathrm{raw}} = \sum_{i=1}^{3} (P_i \times w_i \times 1.05)$$

Cost calculation of raw materials.

Materials	Unit cost (kg^{-1})	EAL	EAL30	EAL30/Zn	EVA
ECHMAE	$8.5	33%	23.3%	22.6%	-
AOMO	$12	50%	35%	34%	-
LMA	$6	17%	11.7%	11.4%	-
CL	$5	-	30%	29%	-
$ZnCl_2$	$8	-	-	3%	-
EVA	$3	-	-	-	74.8%
Paraffin lasticizer	$2	-	-	-	15%
Rosin glyceride	$4.5				10%
Antioxidant	$15	-	-	-	0.2%

Note: The ratio is a mass percentage. The actual feeding should take into account the loss (+5%).

The energy cost

The energy cost is calculated based on the average price of industrial electricity in China at \$0.12 kWh^{-1}, and the actual energy utilization rate is 80%.

The energy cost for preparing photopolymer.

Process	Equipment	Efficiency (h kg^{-1})	Consumption	Cost kg^{-1}
Pre-mixed	5 Kw blender	0.2	(5×0.2)/0.8 ×0.12	\$0.15
Ultraviolet curing	10 kW UV system	0.1	(10×0.1)/0.8 ×0.12	\$0.15
Total				\$0.3

The energy cost for preparing EVA.

Process	Equipment	Efficiency (h kg^{-1})	Consumption	Cost kg^{-1}
Banburying	30 kW Internal mixer	0.05	(30×0.05)/0.8 ×0.12	\$0.225
Extrusion	45 kW Single-screw extruder	0.03	(45×0.03)/0.8 ×0.12	\$0.2025
Cooling	5 kW Water circulation system	0.1	(5×0.1)/0.8 ×0.12	\$0.075
Total				\$0.503

Equipment depreciation cost

Equipment depreciation applied the straight-line method over defined lifespans, accounting for an 8% salvage value of initial purchase costs.

$$\text{Annual Depreciation}=\frac{\text{Equipment Purchase Cost-Salvage Value}}{\text{Service Life}}$$

The depreciation expense of equipment EAL.

Equipment	Purchase cost (\$)	Salvage value (8%) (\$)	Annual depreciation (\$)
UV curing system	52,000	4,160	6,834
Mixing reactor	16,000	1,280	2,944
Total	68,000	5,440	9,778

The depreciation expense of equipment EVA.

Equipment	Purchase cost (\$)	Salvage value (8%) (\$)	Annual depreciation (\$)
Banburying	45,000	3,600	4,140
Extrusion	68,000	5,440	6,256
Cooling	15,000	1,200	1,725
Total	128,000	10,240	12,121

Unit depreciation cost

Unit depreciation cost refers to the equipment depreciation expense allocated for each unit of product produced (such as 1 kilogram or 1 cubic meter), which is used to quantify the impact of equipment capital expenditure during the production process on the unit product cost. The core of it is to evenly distribute the annual depreciation expense of the equipment to the annual output, reflecting the contribution of equipment investment to the cost per piece.

$$\text{Unit depreciation cost} = \frac{\text{Annual depreciation}}{\text{Annual production volume}}$$

$$\text{Unit depreciation cost (EAL30/Zn)} = \frac{9778}{50000} = 0.19556$$

$$\text{Unit depreciation cost (EVA)} = \frac{12121}{200000} = 0.061$$

The depreciation cost of EAL30/Zn is 3.2 times higher than EVA's, mainly attributable to its specialized equipment requirements (particularly UV curing systems) and significantly smaller production capacity (50 tons year^{-1} versus EVA's 200 tons year^{-1}), which limits economies of scale.

Unit depreciation cost

EAL30/Zn: Carbon tax credit (-\$0.12) + wastewater treatment (\$0.12) + additional wastewater treatment (\$0.10) = -\$0.02 kg^{-1} (net environmental benefit).

EVA: VOC treatment (\$0.80) + wastewater treatment (\$0.80) + secondary wastewater treatment (\$0.30) + carbon tax (\$0.18) = \$1.28 kg^{-1} (net environmental cost).

Packaging and transportation

The packaging and transportation costs for photopolymers are relatively high at \$0.72 kg^{-1} due to small-scale production, primarily attributed to small packaging units and limited distribution scale. In contrast, EVA's bulk transportation in large-scale production significantly reduces its unit cost to \$0.48 kg^{-1}, demonstrating the economies of scale effect.

Comparative production cost breakdown of EAL, EAL30, EAL30/Zn and EVA.

Cost item (Kg^{-1})	EAL	EAL30	EAL30/Zn	EVA
Raw materials	\$9.285	\$8.3823	\$8.375	\$3.024
Energy	\$0.30	\$0.30	\$0.30	\$0.503
Equipment depreciation	\$0.19556	\$0.19556	\$0.19556	\$0.061
Environmental cost	-\$0.12	-\$0.12	-\$0.12	\$1.28
Packaging & transportation	\$0.72	\$0.72	\$0.72	\$0.48
Total	\$10.48	\$9.58	\$9.57	\$5.35

Net present value (NPV) and internal rate of return (IRR) analysis

Financial viability was assessed via NPV and IRR calculations using a 10% discount rate, 10-year project horizon, and salvage value recovery, with annual net cash flows (NCF) determined as revenue minus operational expenses. Take the trial-and-error method combined with the interpolation method as an example to calculate the IRR step by step. The standard comprehensive cost-plus method for assumed selling prices, the market benchmarking method, and the value pricing method.

Initial investment (C_0)

The total capital expenditure for EAL equipment amounts to $68,000, comprising a UV curing system ($52,000) and two mixing reactors ($16,000). For EVA production, the equipment purchases cost totals $128,000.

Net cash flow (NCF)

Annual NCF represents the actual net cash inflow generated by an enterprise or project within one year and is a key indicator for evaluating profitability and debt-paying ability.

$$NCF=CI-CO$$

CI*:* Cash inflows; CO: Cash outflows

Net present value (NPV)

The total discounted net cash flow generated by the project throughout its life cycle is calculated through the net present value to determine whether the project is worth investing in. The NPV result is positive and the project is feasible.

$$NPV=\sum_{t=0}^{n}(CI_t-CO_t)(1+i_0)^{-t}$$

CI_t: Cash inflow in year t; CO_t: Cash outflow in year t; i_0: Discount rate (10%); n: Project cycle (10 year)

Present value interest factors of annuity (PVIFA)

The present value coefficient of an annuity is a coefficient used to calculate the present value of a series of future equal cash flows (annuities) at the current point in time. It reflects the total present value of the cash flow of 1 yuan paid (or received) in each period under a specific discount rate (or interest rate) and the number of periods.

$$PVIFA\ (r, n) = \frac{1-(1+r)^{-n}}{r}$$

r: Discount rate per period; n: Period number

Present value factor (PVF)

Calculate the multiplier of the present value of future single cash flows at the current point in time through PVF. It reflects how much 1 yuan at a given discount rate (or interest rate) and period is equivalent to now at a certain point in the future.

$$PVF\ (r, n) = \frac{1}{(1+r)^n}$$

Internal rate of return (IRR)

By adjusting the discount rate IRR, the sum of the present values of all future cash flows exactly offsets the initial investment (NPV=0). At this point, the IRR is the actual rate of return of the project.

$$NPV\ (IRR) = \sum_{t=0}^{n}\frac{C_t}{(1+IRR)^t}=0$$

Key financial indicators of EAL, EAL30, EAL30/Zn and EVA.

Process	EAL	EAL30	EAL30/Zn	EVA
C_0	68,000	68,000	68,000	128,000
NCF	226048	271,000	521500	371500
PVIFA (r, n)	6.1446	6.1446	6.1446	6.1446
PVF (r, n)	0.3855	0.3855	0.3855	0.3855
NPV	1323078	1,599,425	2217149	3132585
IRR	58%	62%	75%	35%

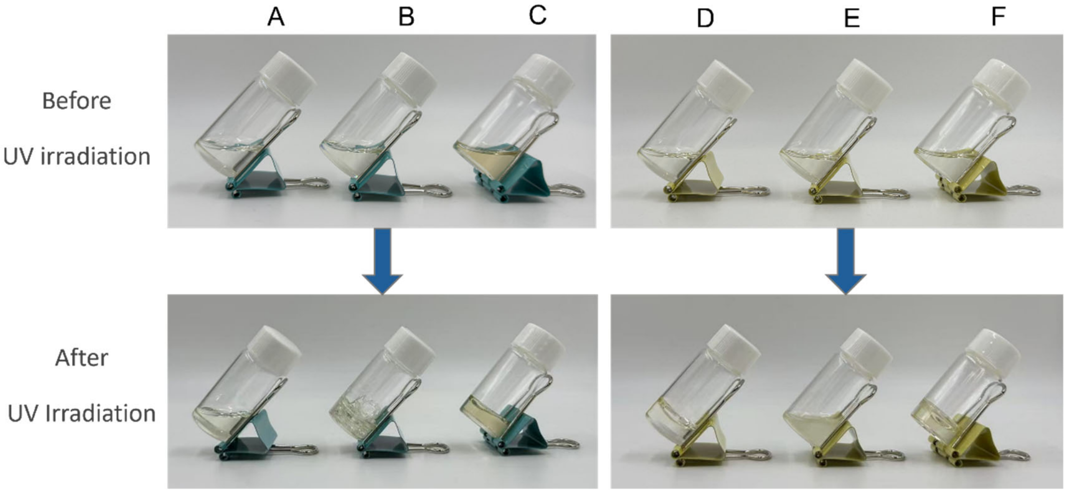

Supplementary Fig. 1. Macroscopic curing behavior of individual monomers and binary formulations before and after UV irradiation.

A ~ C show single-component systems of ECHMAE, AOMO, and LMA, respectively. D ~ F present binary mixtures of AOMO/LMA, ECHMAE/LMA, and ECHMAE/AOMO. Only acrylate-containing systems form shape-stable solids upon UV curing, whereas ECHMAE alone remains non-self-supporting, highlighting the essential role of rapid acrylate polymerization in establishing the primary network scaffold.

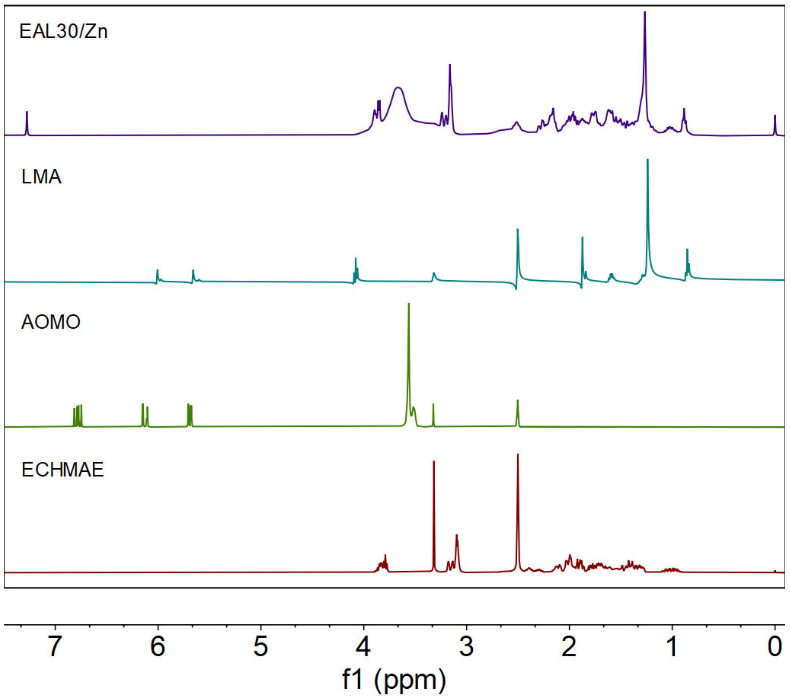

Supplementary Fig. 2. 1H NMR of ECHMAE, AOMO, LMA and EAL30/Zn.

The structural evolution of the resin during ultraviolet curing was examined by 1H NMR spectroscopy. As shown in Fig. S2, the spectra of the individual monomers display characteristic resonances associated with vinyl groups and epoxy moieties, whereas these features are largely absent after curing. Instead, the cured EAL30/Zn resin exhibits broadened signals characteristic of ether-rich environments, consistent with extensive network formation. The disappearance of vinyl and epoxy resonances, together with the emergence of polyether-related signals, confirms the concurrent progression of acrylate radical polymerization and Zn^{2+}-mediated epoxy ring opening. These transformations collectively lead to the formation of an interpenetrating polyacrylate/polyether network.

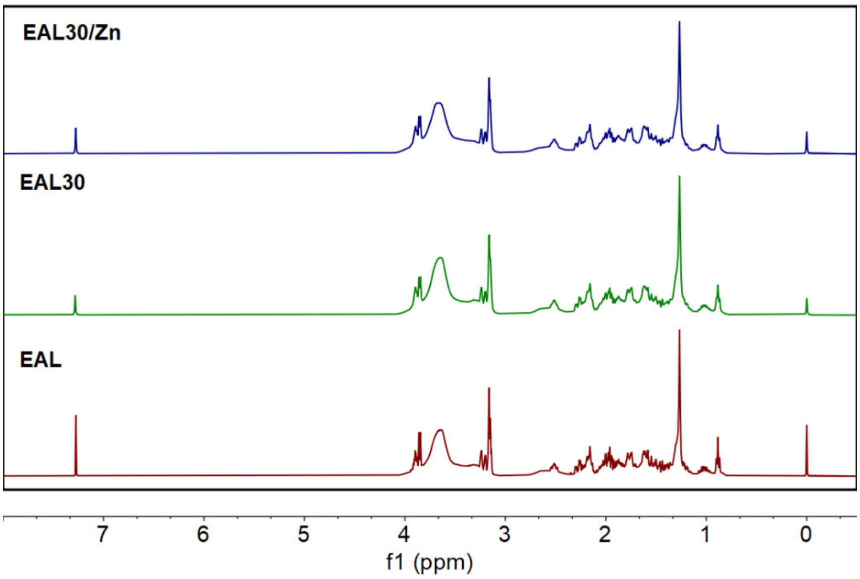

Supplementary Fig. 3. 1H NMR of EAL, EAL30, EAL30/Zn.

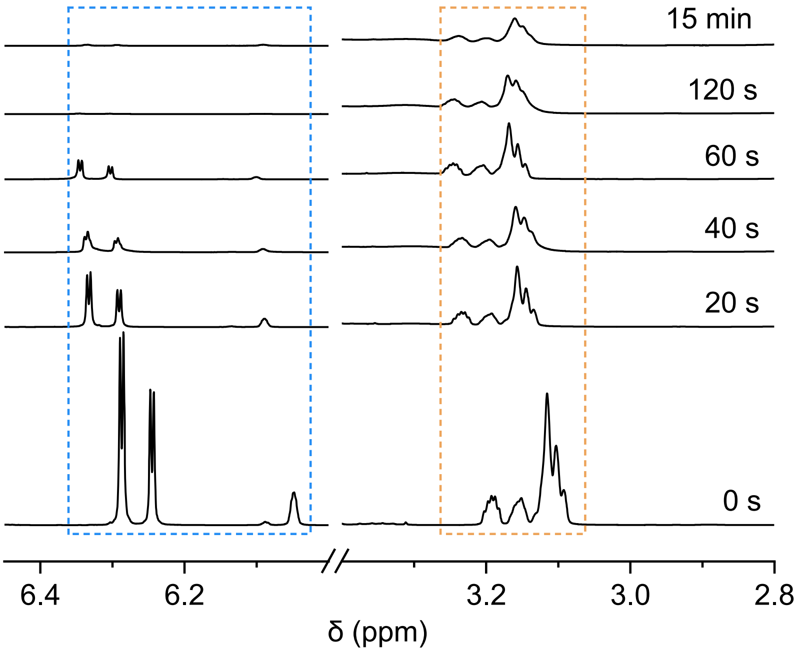

Supplementary Fig. 4. Time-resolved ^{1}H NMR spectra of EAL acquired during UV curing, normalized against the inert LMA terminal -CH$_3$ protons.

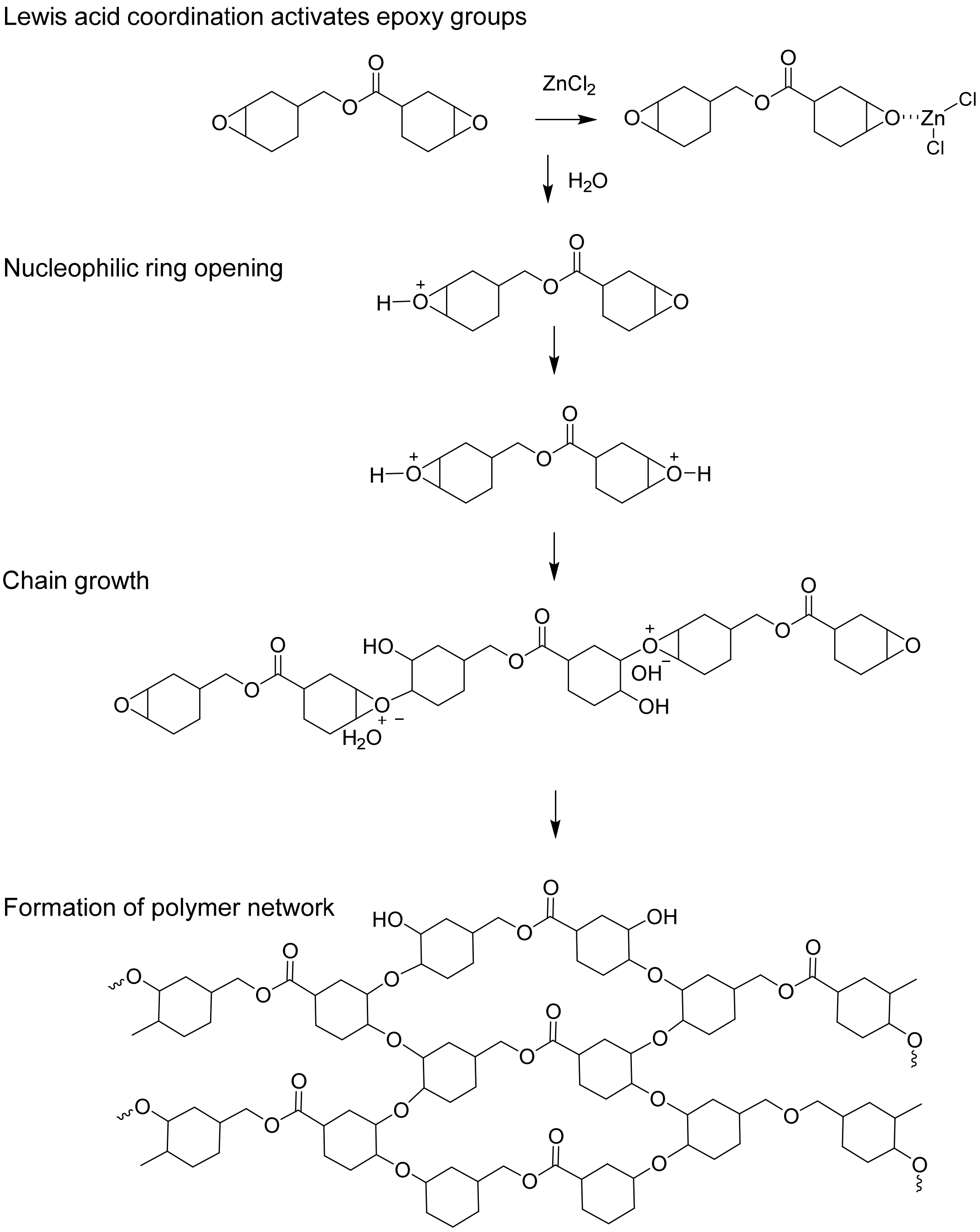

Supplementary Fig. 5. Schematic illustration of the Lewis-acid-assisted epoxy ring-opening mechanism in the dual-curing system.

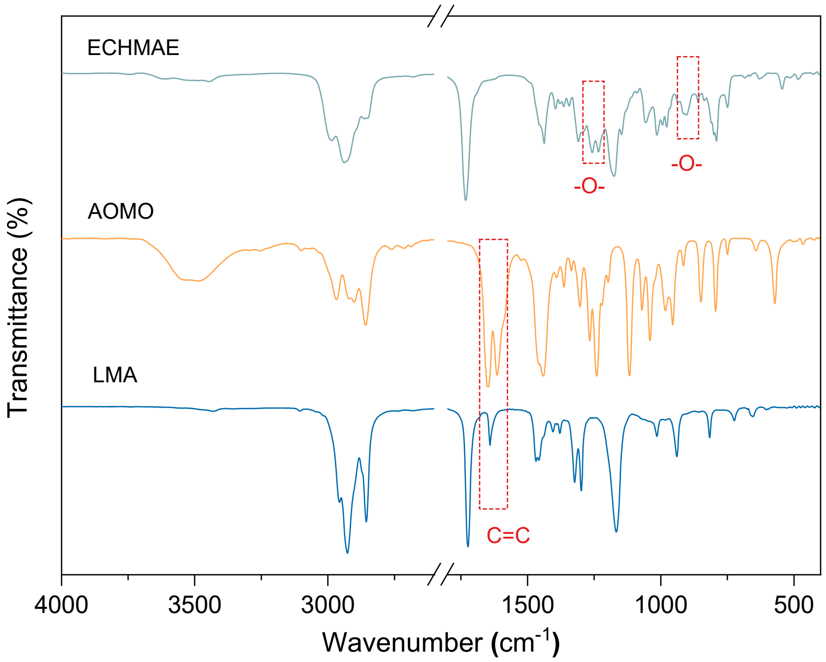

Supplementary Fig. 6. FT-IR spectra of ECC, AOMO and LMA.

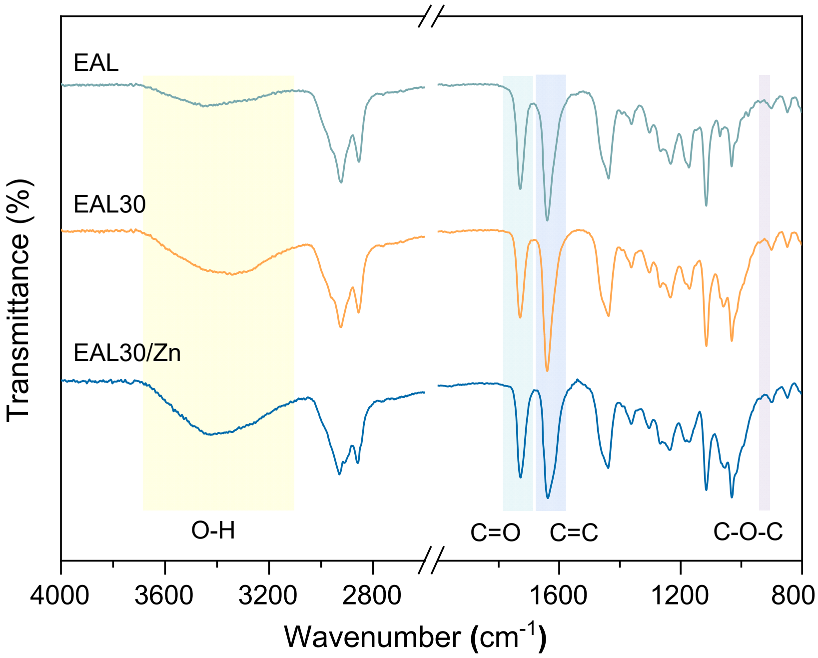

Supplementary Fig. 7. FTIR spectra of EAL, EAL30, and EAL30/Zn.

The FTIR spectra reveal the multiscale network evolution induced by cellulose and Zn^{2+}. The strengthened and red-shifted O–H band confirms the formation of an extensive hydrogen-bonding network, while the disappearance of the C=C peak indicates complete acrylate conversion. The substantial attenuation of the epoxy C–O–C band in EAL30/Zn demonstrates Zn^{2+}-assisted epoxy ring opening, leading to the formation of a secondary polyether network (1). These spectral features collectively verify the construction of an interpenetrating and coordination-enhanced architecture in EAL30/Zn.

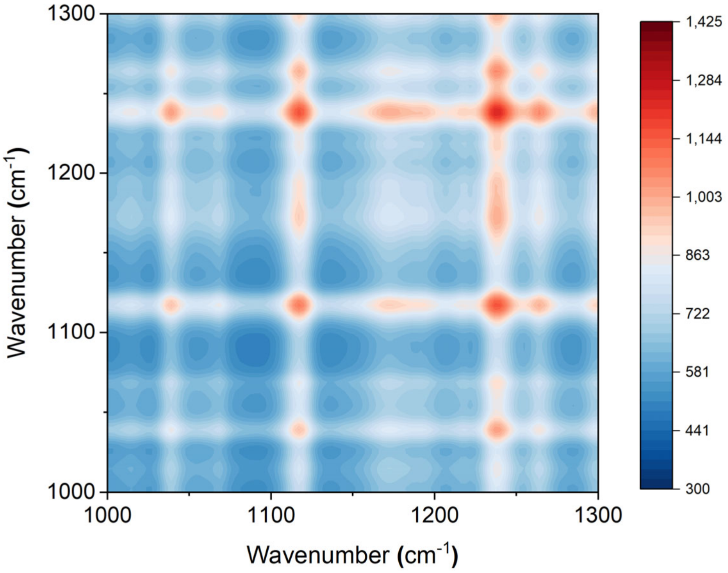

Supplementary Fig. 8. Time-dependent synchronous 2D-COS IR maps of the EAL30/Zn.

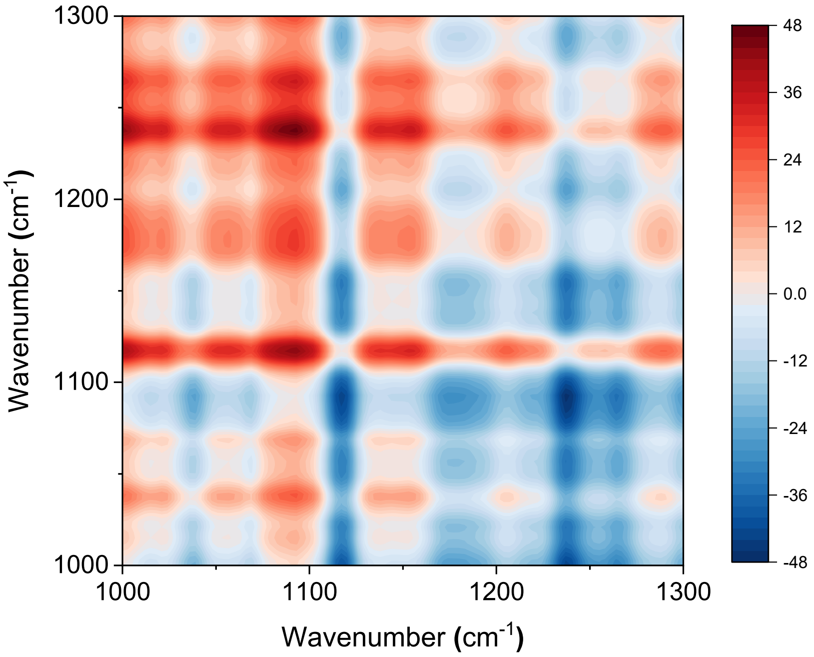

Supplementary Fig. 9. Time-dependent asynchronous 2D-COS IR maps of the EAL30/Zn.

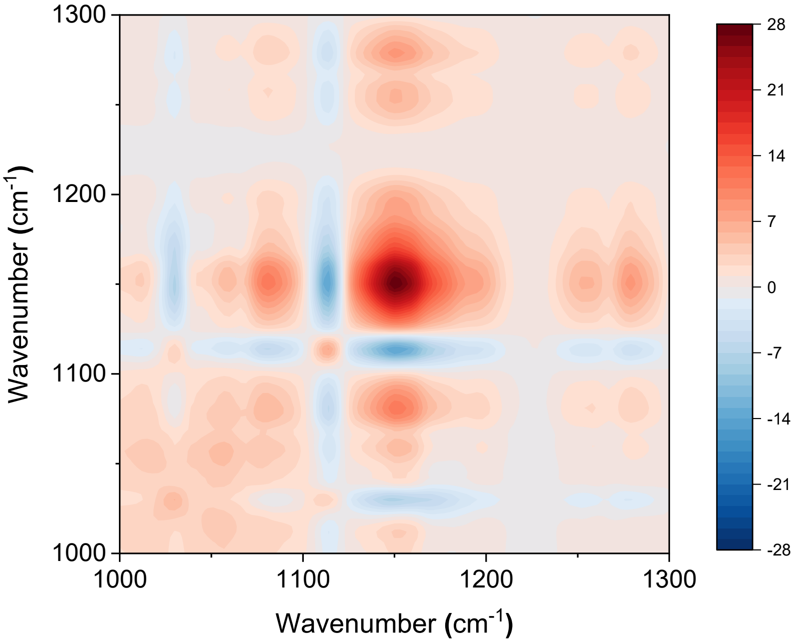

Supplementary Fig. 10. Composition-dependent synchronous 2D-COS IR maps generated using Zn^{2+} content as the external perturbation.

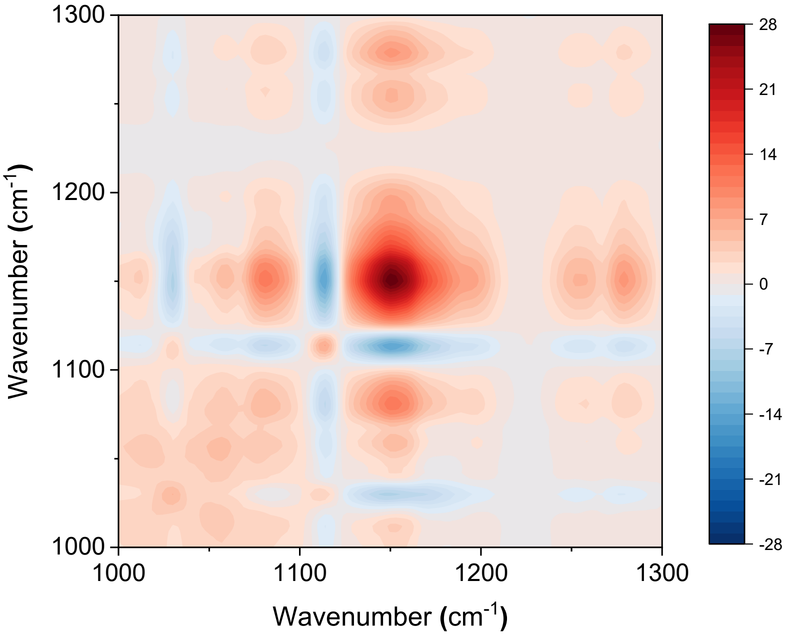

Supplementary Fig. 11. Composition-dependent asynchronous 2D-COS IR maps generated using Zn^{2+} content as the external perturbation.

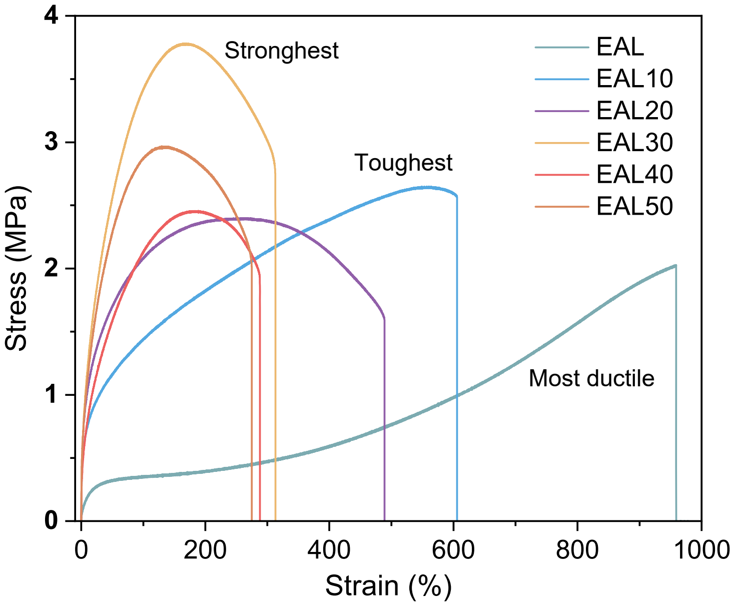

Supplementary Fig. 12. Stress–strain curves of EAL ~ EAL50.

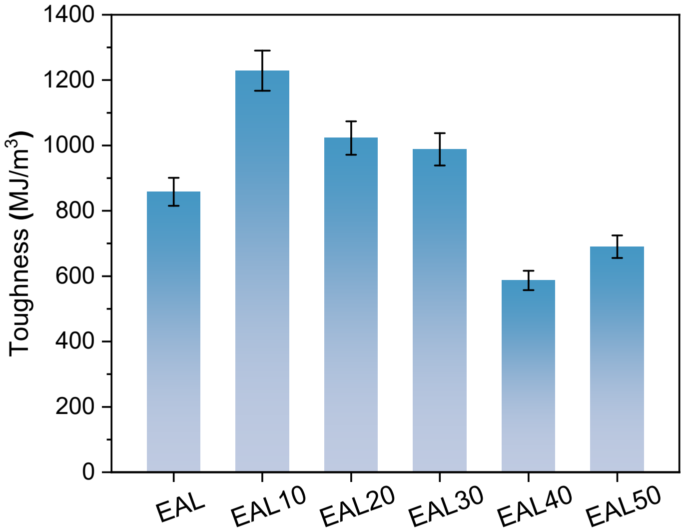

Supplementary Fig. 13. Comparison of toughness between EAL ~EAL50.

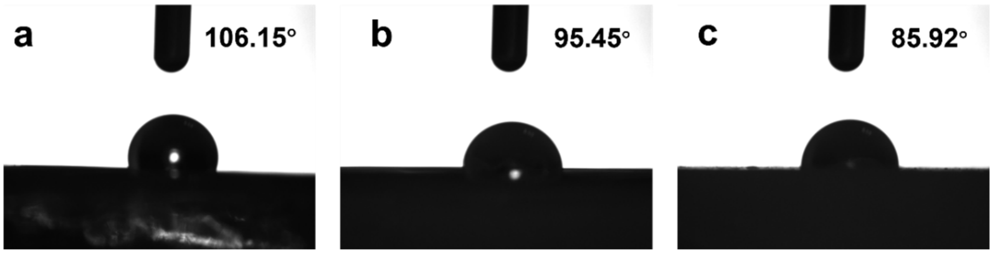

Supplementary Fig. 14. The water contact angle of adhesive (a) EAL, (b) EAL30, and (c) EAL30/Zn3%.

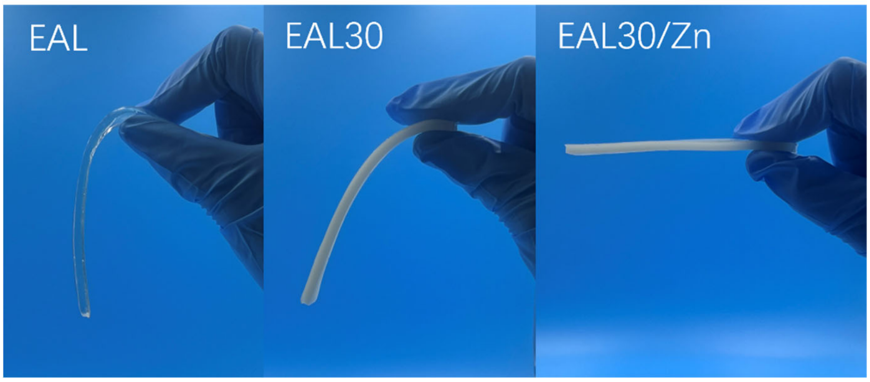

Supplementary Fig. 15. Images of EAL, EAL30 and EAL30/Zn.

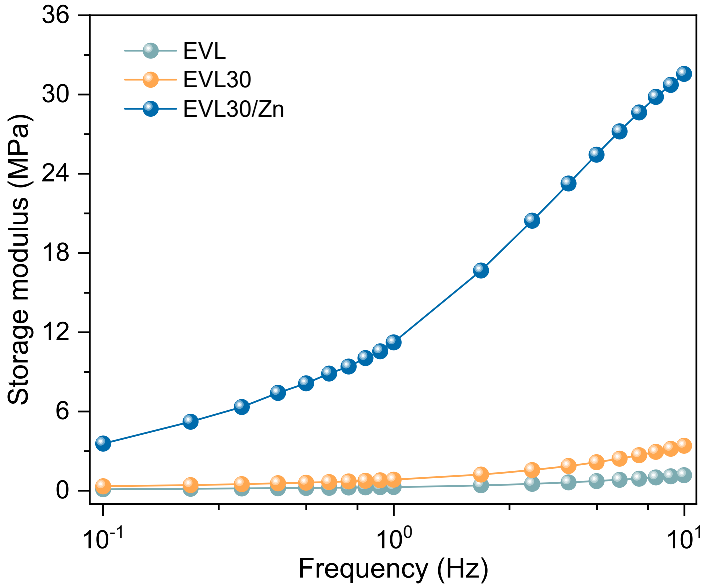

Supplementary Fig. 16. Storage modulus as a function of vibration frequency.

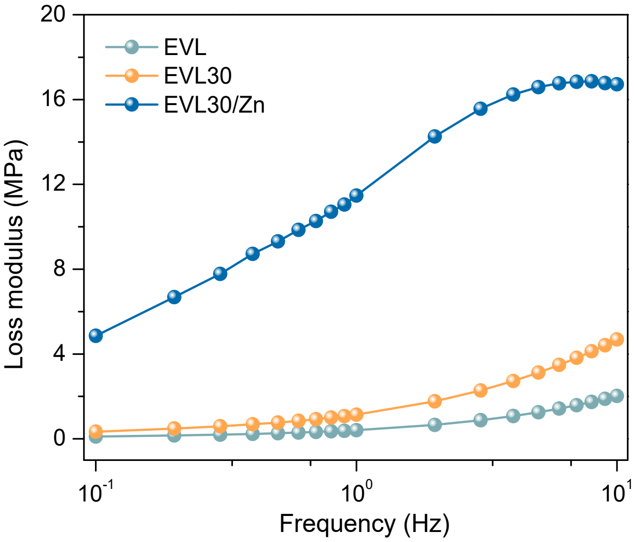

Supplementary Fig. 17. Loss modulus as a function of vibration frequency.

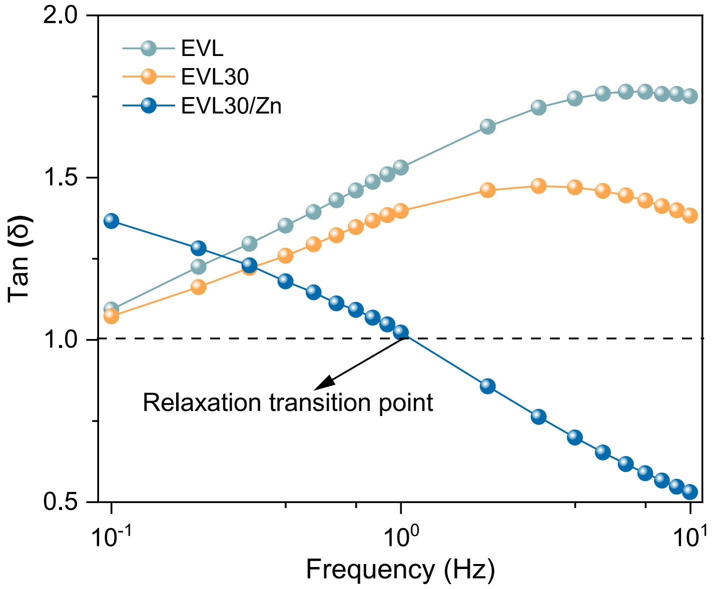

Supplementary Fig. 18. Tan δ as a function of vibration frequency.

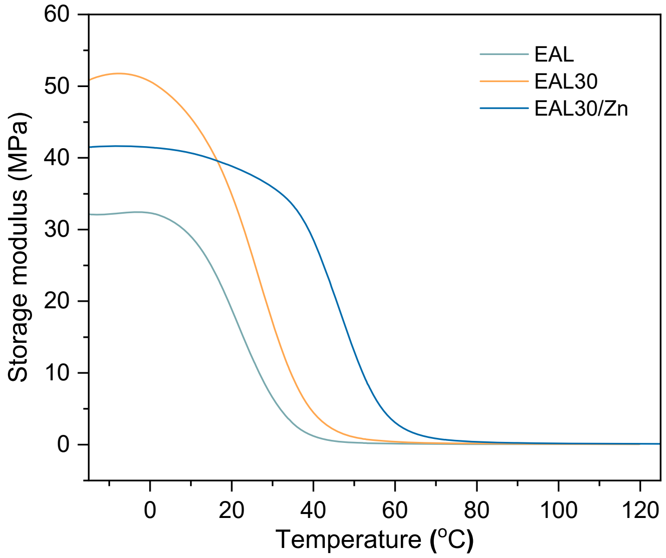

Supplementary Fig. 19. Storage modulus as a function of temperature.

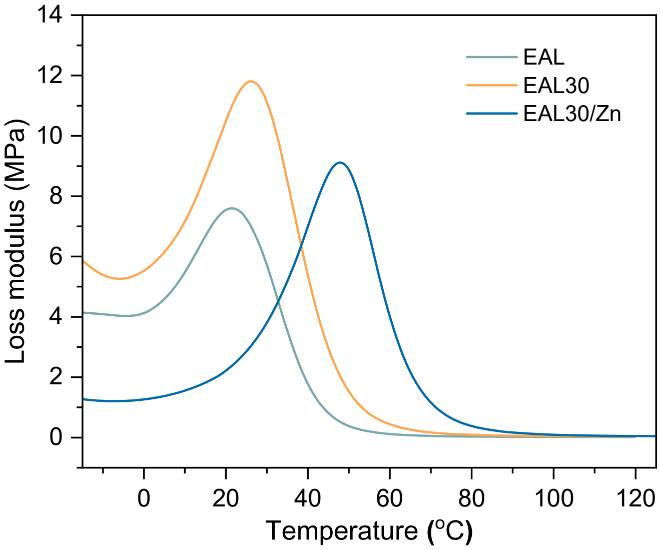

Supplementary Fig. 20. Loss modulus as a function of temperature.

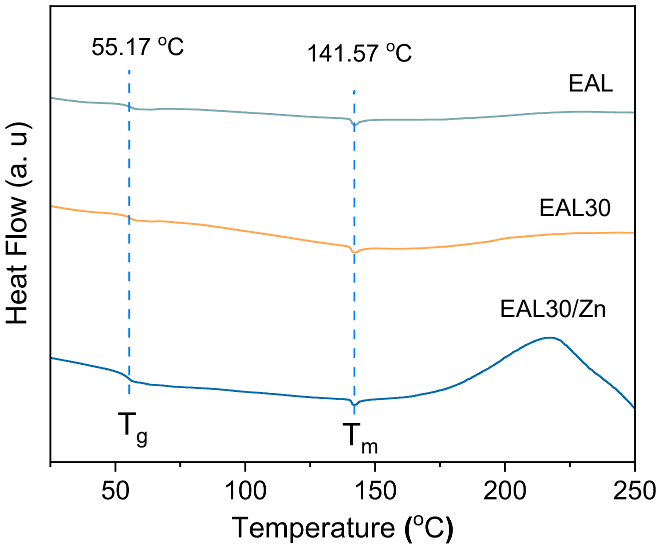

Supplementary Fig. 21. Differential scanning calorimetry (DSC) test of photopolymers.

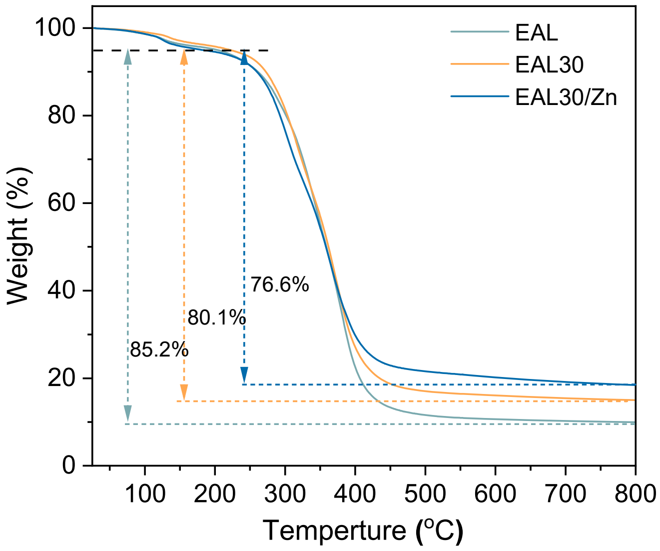

Supplementary Fig. 22. Thermogravimetric (TG) test of photopolymers.

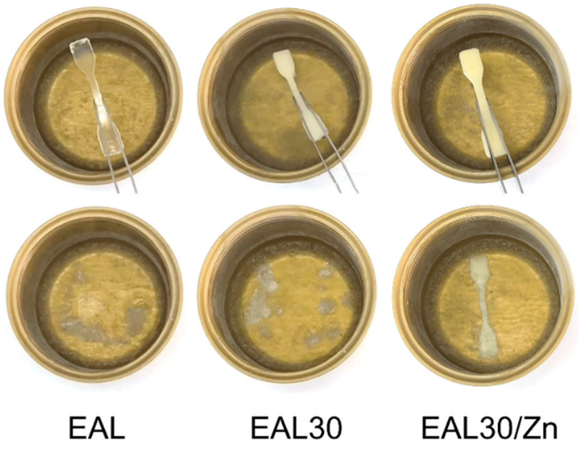

Supplementary Fig. 23. EAL, EAL30 and EAL30/Zn hot melts tested for freeze resistance in liquid nitrogen.

Under cryogenic conditions, EAL fractured within 2 s, EAL30 extended durability to ≈ 10 s, and EAL30/Zn maintained structural integrity for ≈ 300 s.

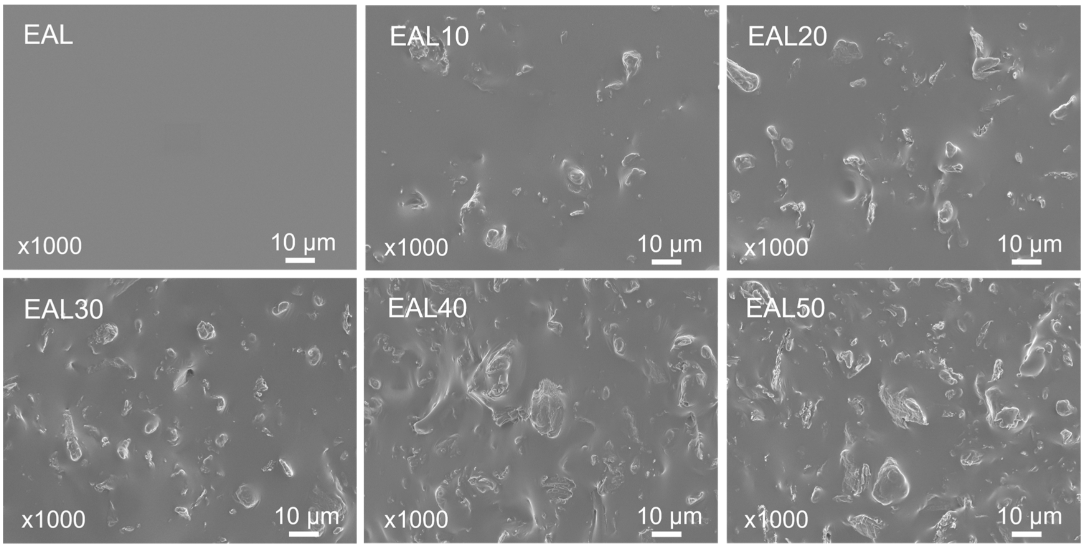

Supplementary Fig. 24. SEM images of the fracture surfaces of EAL, EAL10, EAL20, EAL30, EAL40, and EAL50.

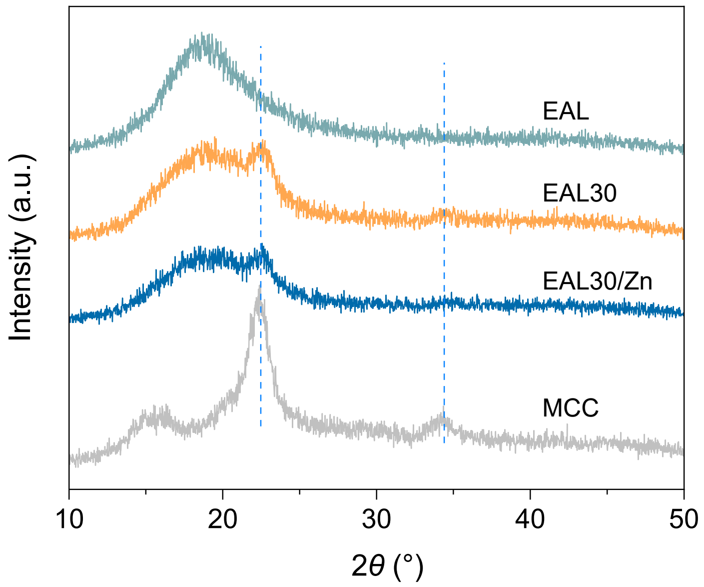

Supplementary Fig. 25. XRD patterns of MCC and photopolymers.

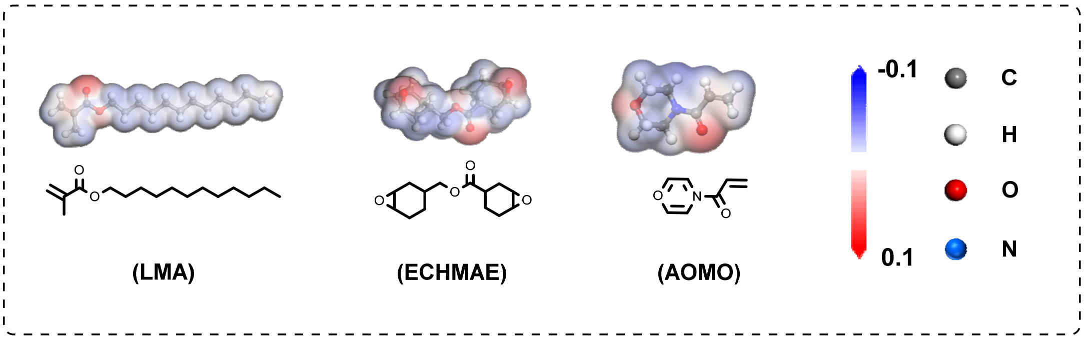

Supplementary Fig. 26. Surface electrostatic potential of the monomer configuration.

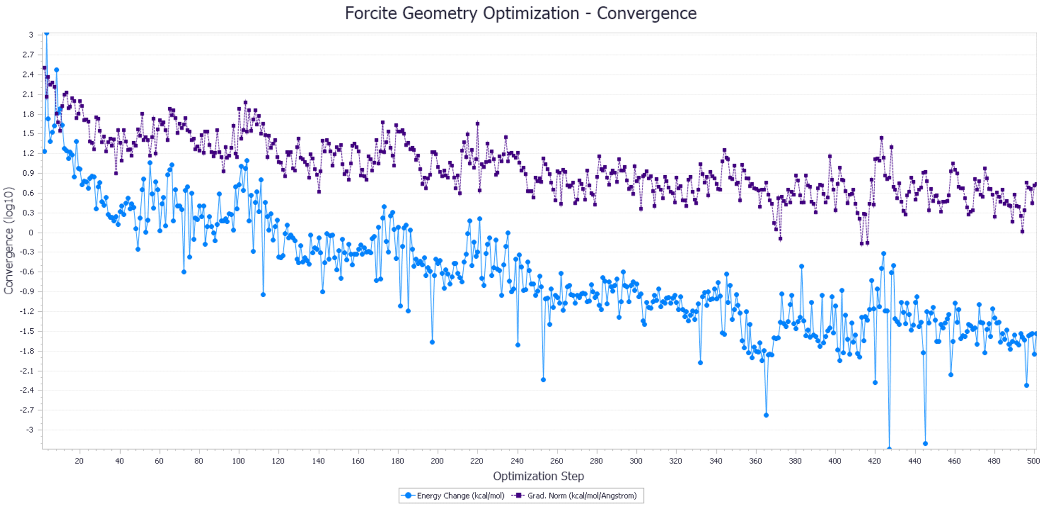

Supplementary Fig. 27. Polymer force field optimization trajectory.

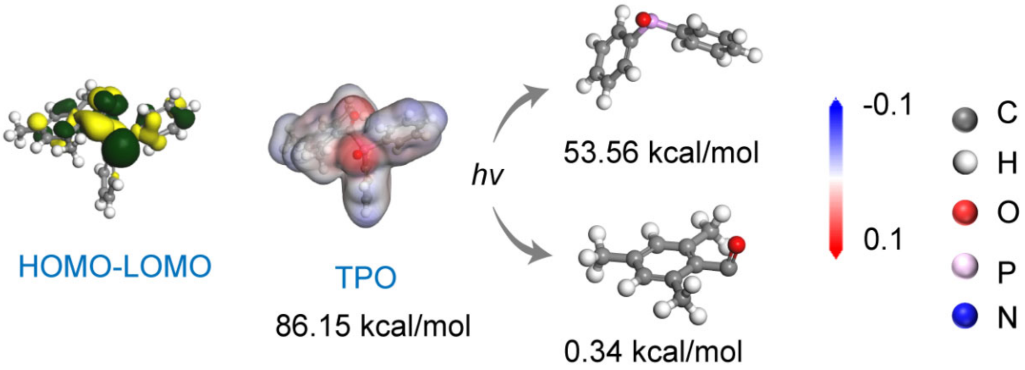

Supplementary Fig. 28. Electronic structure and photolysis of TPO.

TPO molecules underwent electronic transitions after absorbing ultraviolet light, leading to the excitation of their ground-state electrons to a high-energy state (2). As a result, this process significantly increased the total energy of the molecules. According to quantum chemical calculations, the single-point energy of the optimized TPO molecule was found to be 86.15 kcal mol. Subsequently, following homolytic cleavage of the C–P=O bond, two free radicals were generated, with energies of 53.56 kcal/mol (diphenylphosphine free radical, E1) and 0.34 kcal mol-1 (benzoyl free radical, E_2), respectively. Further kinetic analysis revealed that the highly reactive diphenylphosphine radical (E1) played a predominant role in chain-growth reactions due to its elevated energy and reactivity29. In contrast, the low-energy benzoyl oxide radical (E2) primarily participated in chain termination reactions. Specifically, the radical underwent an addition reaction with the acryloyl double bond of AOMO, generating a new radical intermediate. The carbon-carbon double bonds of other AOMO or LMA monomers could be further reacted by this intermediate, and the polymer chain was continuously extended through a chain-growth mechanism, ultimately forming a high-molecular-weight polymer chain. Thus, this distinct characteristic of free radical behavior provided an essential foundation for controlling the polymerization process.

The energy change (ΔE) of the homolytic reaction was calculated by the difference between the energy of the free radical and the total energy of TPO:

$$\Delta E = E_1 + E_2 - E_{TPO}$$

The calculated ΔE of -32.25 kcal/mol indicated that this homolytic reaction was a thermodynamically spontaneous and exothermic process, favoring the formation of free radicals.

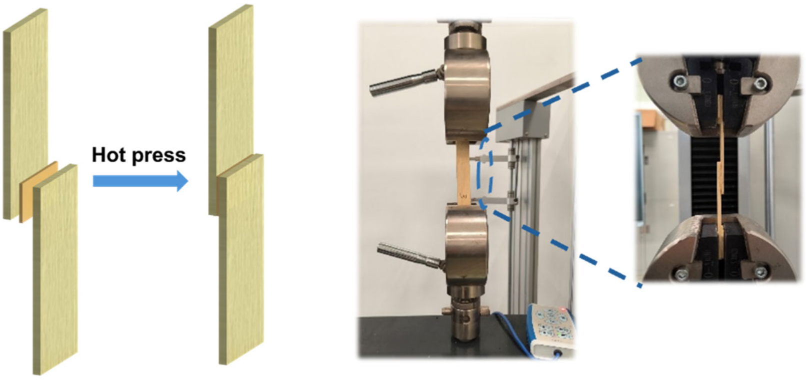

Supplementary Fig. 29. Schematic illustration of hot-press bonding and the lap-shear testing setup.

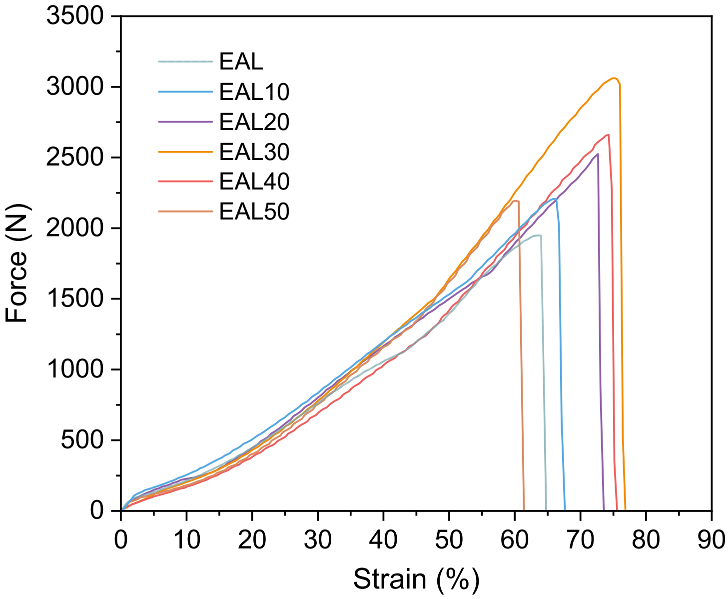

Supplementary Fig. 30. Force–strain curves obtained from tensile testing of EAL-based samples. Fundamentally, the bonding strength was governed by the cohesive energy of the adhesive together with the interfacial adhesion energy. The hydroxyl functional groups abundant in cellulose molecules could engage in multiple reversible interactions, including hydrogen bonding and van der Waals forces, with the hydroxyl groups present on the substrate surface. Consequently, this interaction significantly enhanced interfacial adhesion. Therefore, increasing the cellulose content within an appropriate range could effectively improve adhesive strength.

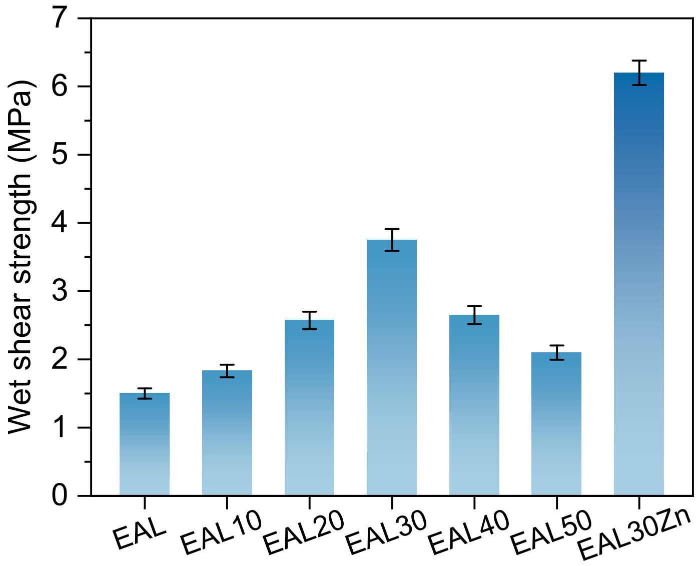

Supplementary Fig. 31. Wet shear strength curves obtained from tensile testing of EAL-based samples.

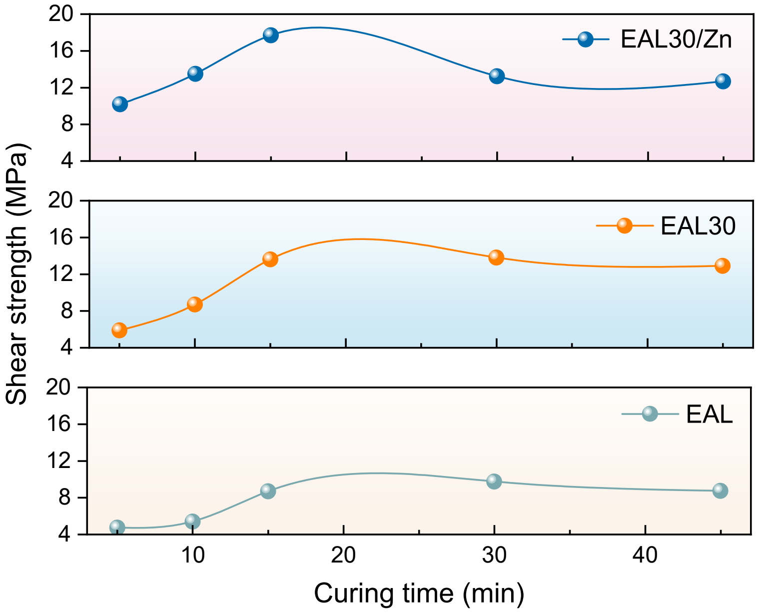

Supplementary Fig. 32. The shear strength of photopolymers with different curing times.

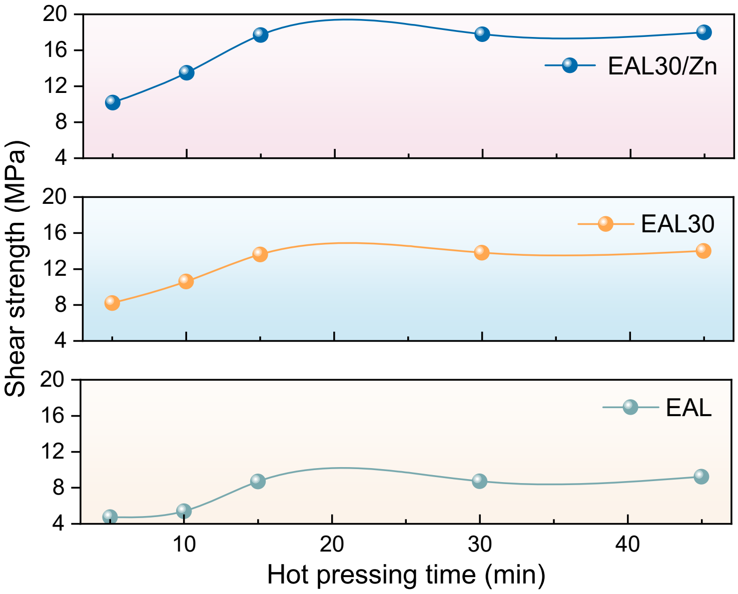

Supplementary Fig. 33. The shear strength of photopolymers with different hot-pressing times.

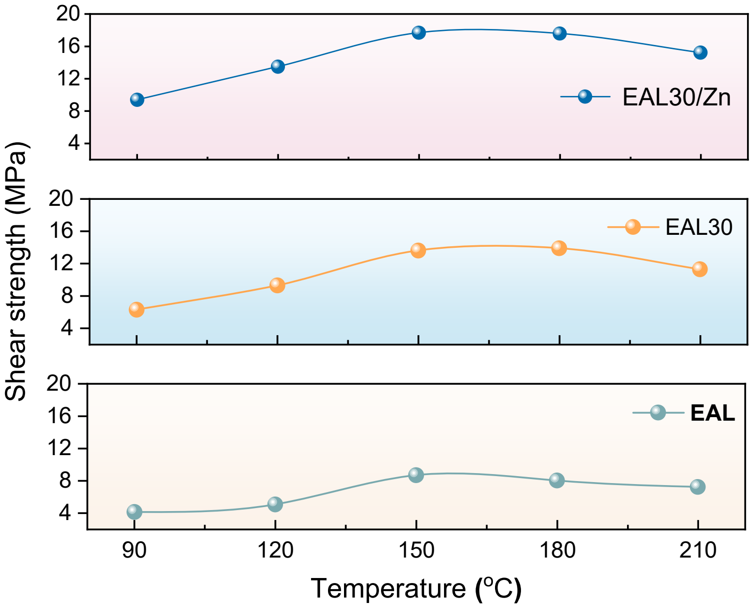

Supplementary Fig. 34. The shear strength of photopolymers with different hot-pressing temperature.

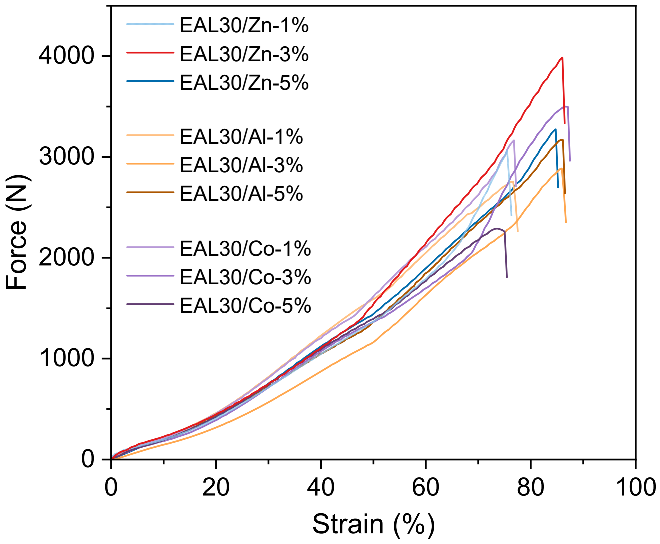

Supplementary Fig. 35. Shear force tests using different metal coordination.

To verify that the enhancement originated from Lewis-acid-assisted epoxy ring-opening rather than a nonspecific ionic effect (figs. 35 and 36), several representative metal ions with different Lewis acid strengths were examined. Among them, Zn^{2+} exhibited the highest adhesion, whereas Al^{3+} with markedly stronger Lewis's acidity and Co^{2+} with moderately stronger acidity produced only limited improvements. This selectivity indicated that Zn^{2+} offered an optimal Lewis acidity window that activated the oxirane group while avoiding over-coordination or excessive network restriction. Consistent with this interpretation, SEM observations revealed that excessive Zn^{2+} loading led to morphological densification and reduced toughness (Fig. 37).

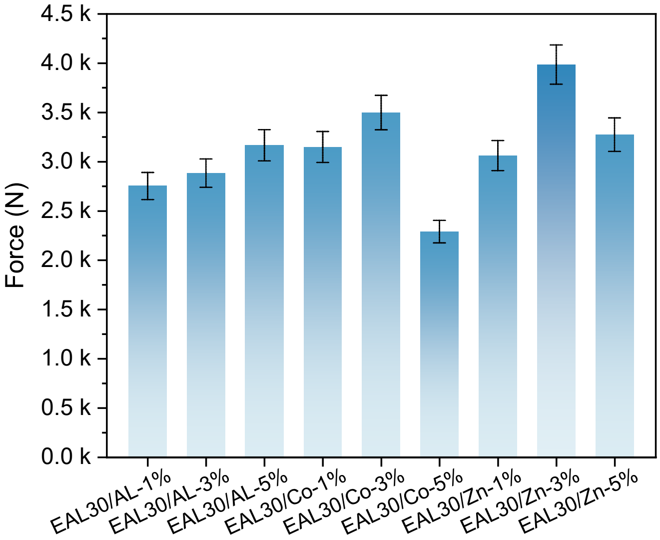

Supplementary Fig. 36. The shear force strength using different metal coordination.

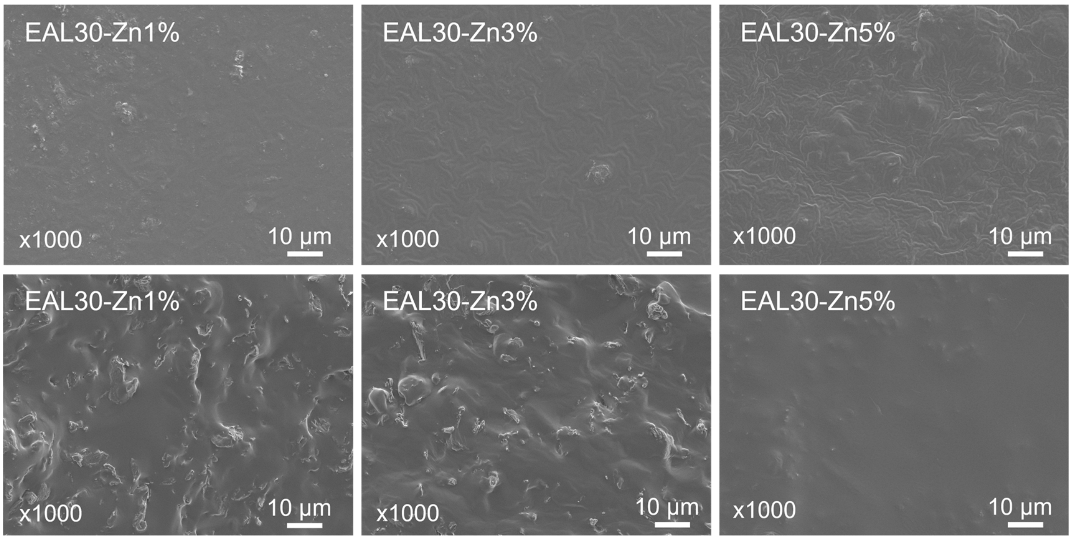

Supplementary Fig. 37. SEM images of surface morphologies and fracture surfaces of EAL30/Zn at Zn^{2+} contents of 1%, 3%, and 5%.

Scanning electron microscopy reveals a clear evolution in surface and fracture morphologies with increasing Zn^{2+} content. At low Zn^{2+} loading (EAL30/Zn1%), the fracture surface is relatively smooth, indicating limited plastic deformation and restricted energy dissipation. At an intermediate Zn^{2+} content (EAL30/Zn3%), the fracture surface becomes markedly rough and features abundant fibrillar structures and crack deflection, suggesting enhanced stress redistribution and effective energy dissipation during fracture. Further increasing the Zn^{2+} content to 5% (EAL30/Zn5%) results in a denser and more uniform fracture morphology, implying an overly constrained network in which excessive crosslinking suppresses large-scale chain mobility. These observations indicate the existence of an optimal Zn^{2+} content that promotes deformation-enabled fracture and synergistic mechanical performance, whereas excessive Zn^{2+} loading leads to morphological densification and reduced toughness (3, 4).

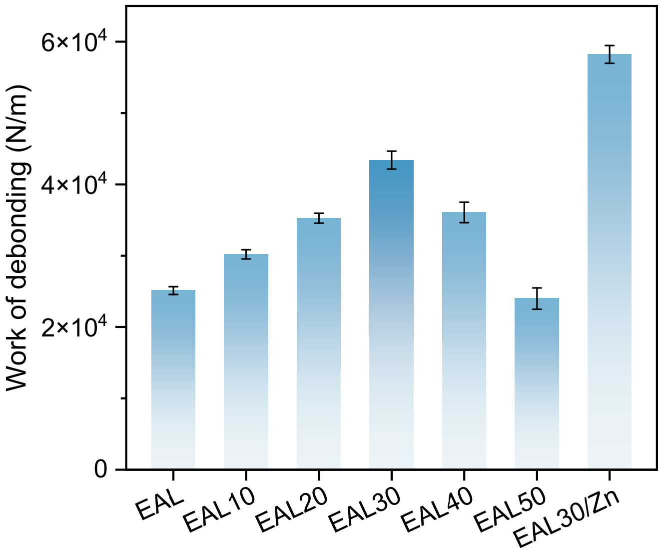

Supplementary Fig. 38. The work of debonding of adhesives.

Supplementary Fig. 39. The pulling test of the wooden board after hot pressing (bonding area 4 cm^2).

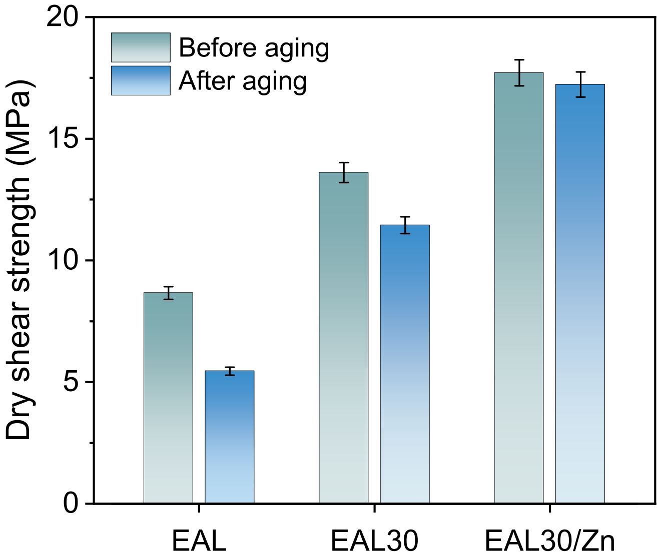

Supplementary Fig. 40. The shear strength of photopolymers before and after ultraviolet aging. After one month of UV irradiation, the EAL adhesive displayed a marked decline in shear strength. In sharp contrast, the EAL30/Zn adhesive maintained outstanding weather resistance, retaining up to 96% of its initial shear strength. Systematic environmental testing further confirmed that EAL30/Zn possessed remarkable stability against combined aging factors, including ultraviolet radiation, elevated temperature, high humidity, and periodic rainwater exposure. Even under repeated damp-heat cycles, the adhesive preserved stable interfacial bonding performance, demonstrating its long-term reliability for outdoor structural applications.

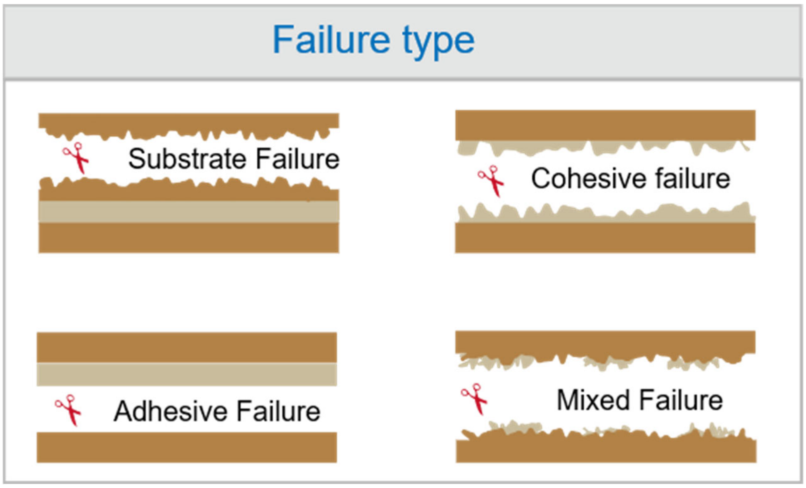

Supplementary Fig. 41. Schematic illustration of four typical adhesion failure modes: substrate failure, cohesive failure, adhesive failure, and mixed failure.

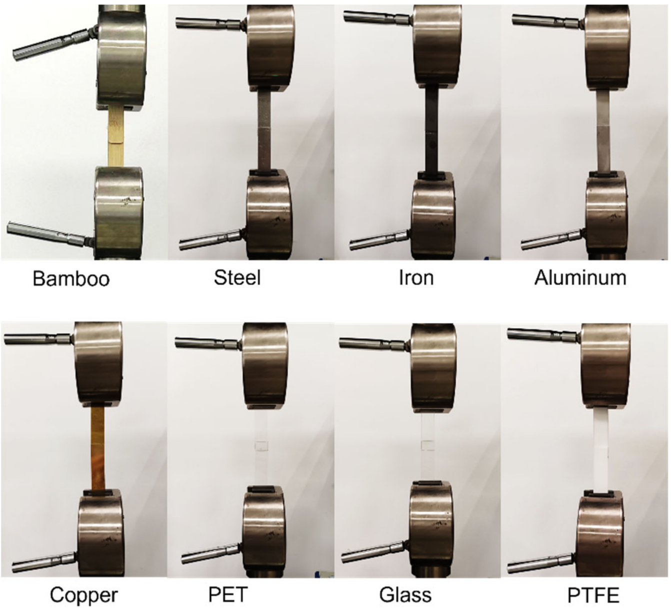

Supplementary Fig. 42. The shear strength of photopolymers with different hot-pressing temperature.

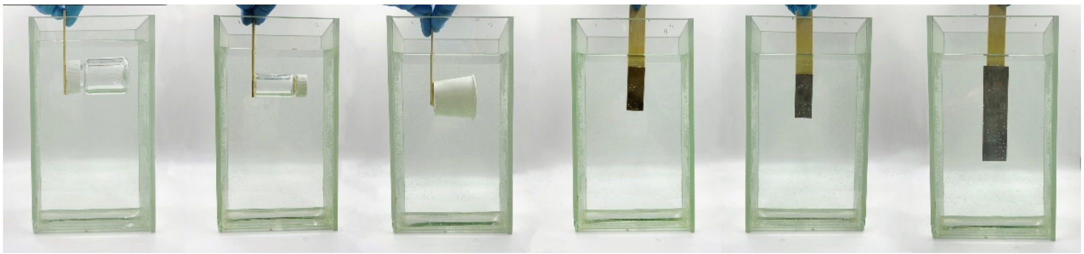

Supplementary Fig. 43. Adhere to various substrates in a water environment.

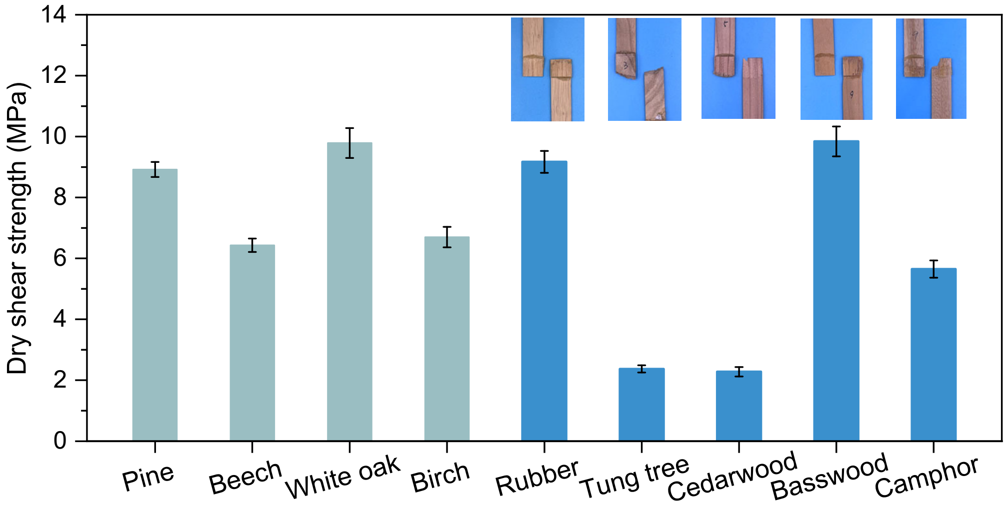

Supplementary Fig. 44. Dry shear strength of bonded joints on different substrates.

To evaluate the substrate generality of the adhesive, shear tests were first conducted on a range of wood species with distinct densities and microstructures. Although measurable bonding strengths were obtained on all substrates, several low-density woods exhibited premature substrate fracture during loading. Thus, bamboo was selected as the model substrate to enable quantitative comparison of adhesive performance, as its high density, aligned fiber structure, and reproducible fracture behavior minimize substrate-dominated failure.

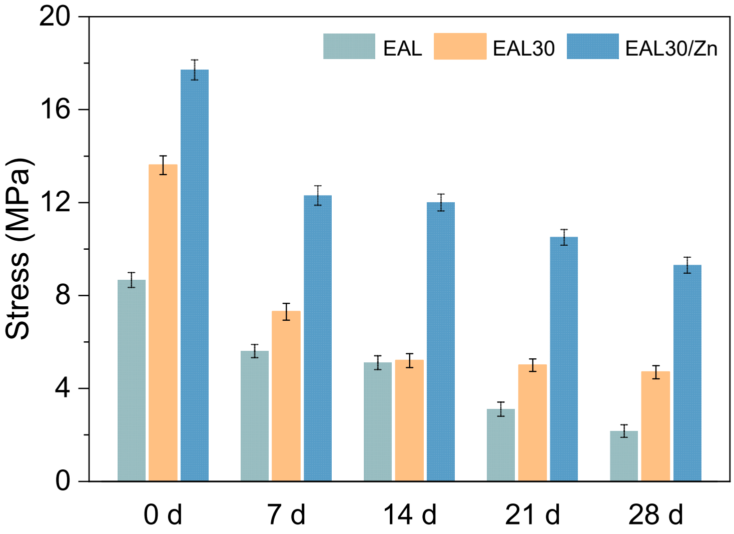

Supplementary Fig. 45. The adhesive strength of EAL, EAL30 and EAL30/Zn in water for 28 days.

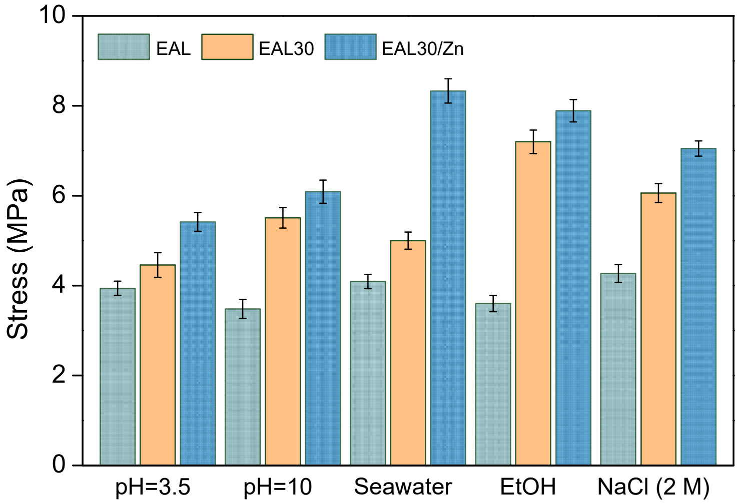

Supplementary Fig. 46. Adhesive strength after soaking in various solvents for 12 hours.

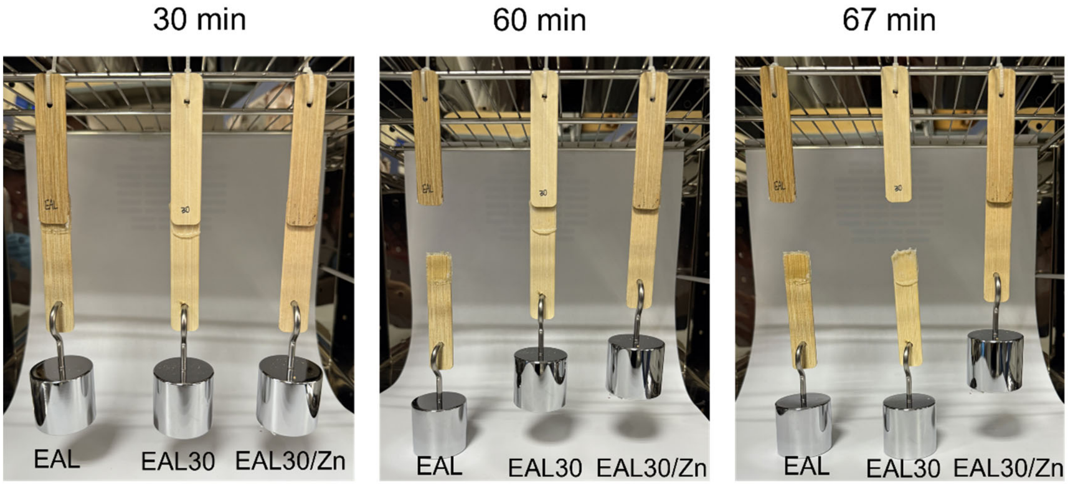

Supplementary Fig. 47. The state of wood chips changing over time when bearing a 500 g weight in a 90 ℃ oven.

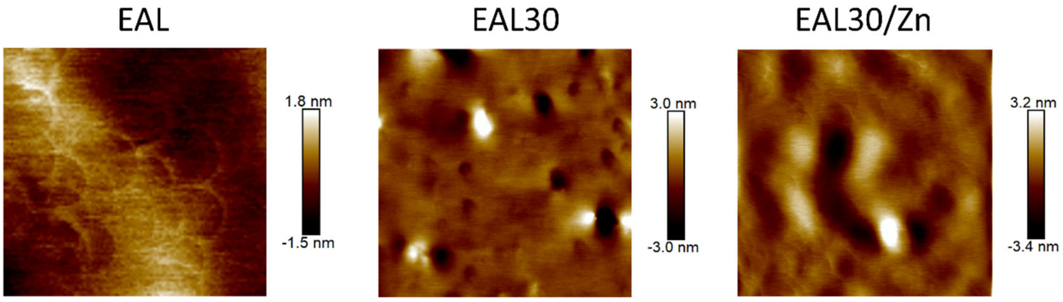

Supplementary Fig. 48. AFM height images of EAL, EAL30, and EAL30/Zn.

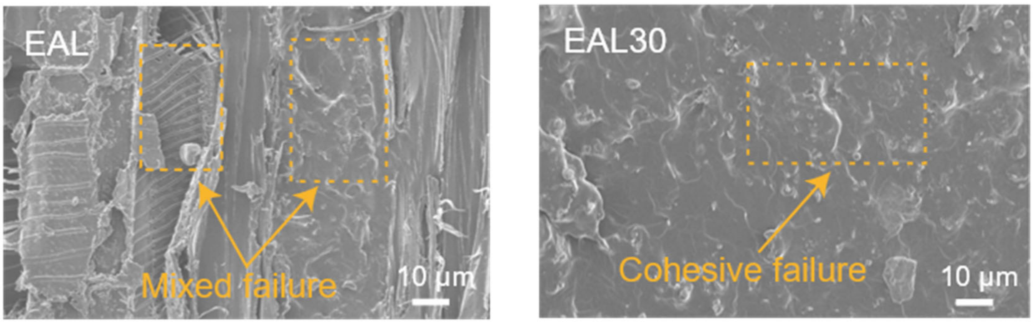

Supplementary Fig. 49. Schematic diagram of interfacial adhesion of adhesive to the surface of bamboo and SEM image of the fracture.

Supplementary Fig. 50. The EAL30/Zn adhesive experienced substrate fracture during the test.

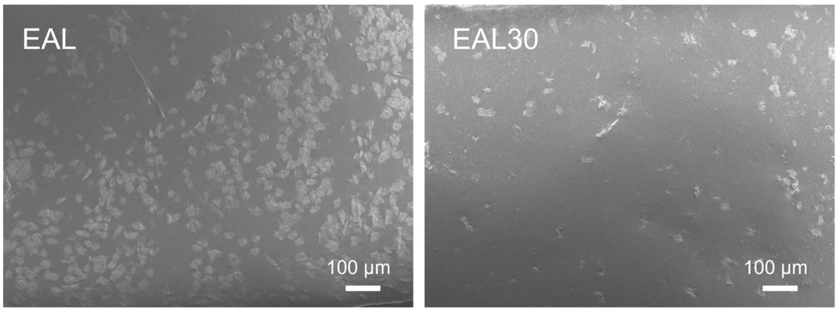

Supplementary Fig. 51. SEM surface morphologies of EAL and EAL30 after tensile deformation.

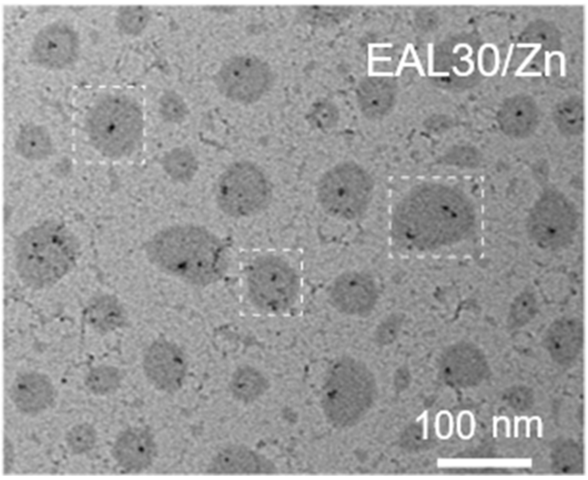

Supplementary Fig. 52. Transmission electron microscopy (TEM) image of the EAL30/Zn resin.

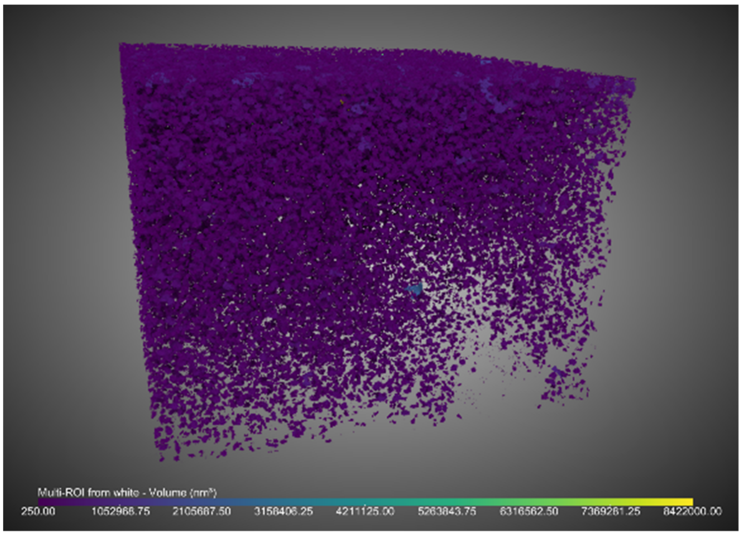

Supplementary Fig. 53. Three-dimensional reconstruction of segmented features in the EAL30/Zn resin obtained by FIB–SEM tomography.

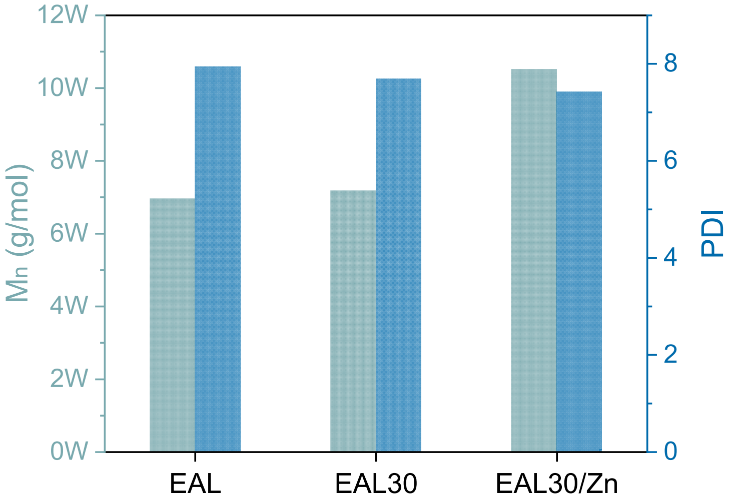

Supplementary Fig. 54. Number-average molecular weight (Mn) and polymer dispersity index (PDI) of photopolymers.

Supplementary Fig. 55. Photograph of a 3D-printed object fabricated by stereolithography.

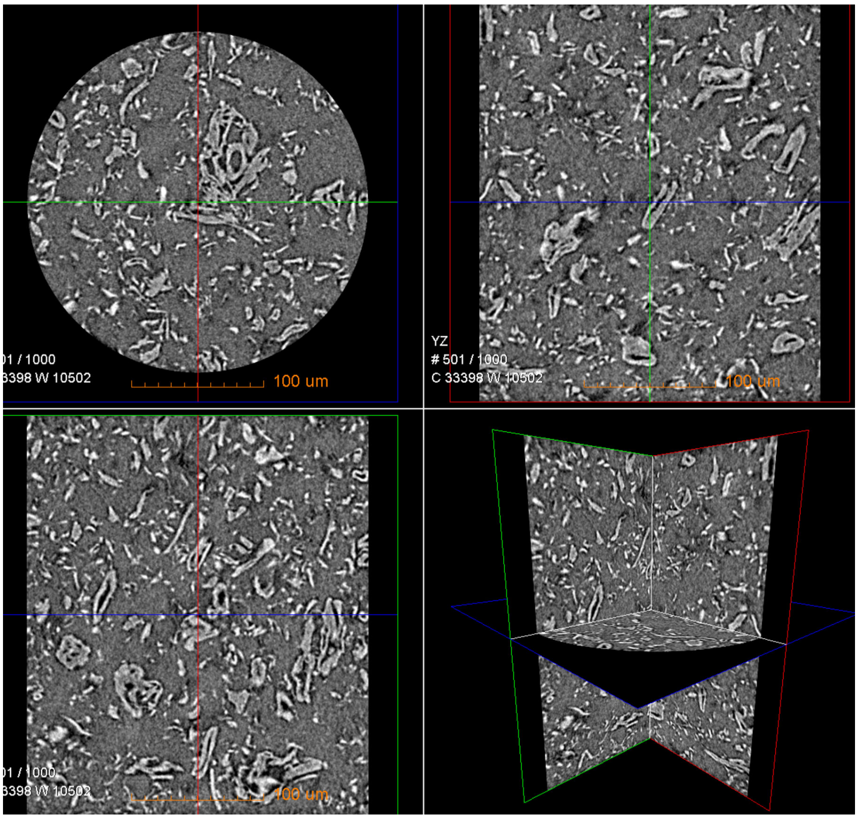

Supplementary Fig. 56. XRM reconstruction of the EAL sample acquired at a voxel resolution of 0.3 μm.

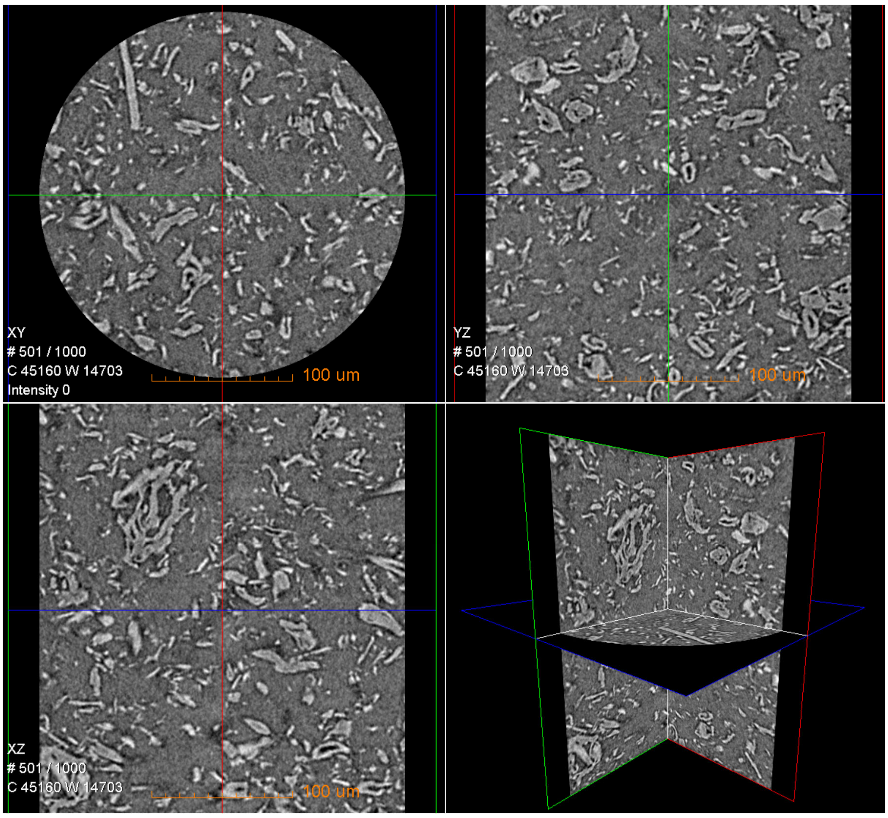

Supplementary Fig. 57. XRM reconstruction of the EAL/Zn sample acquired at a voxel resolution of 0.3 μm.

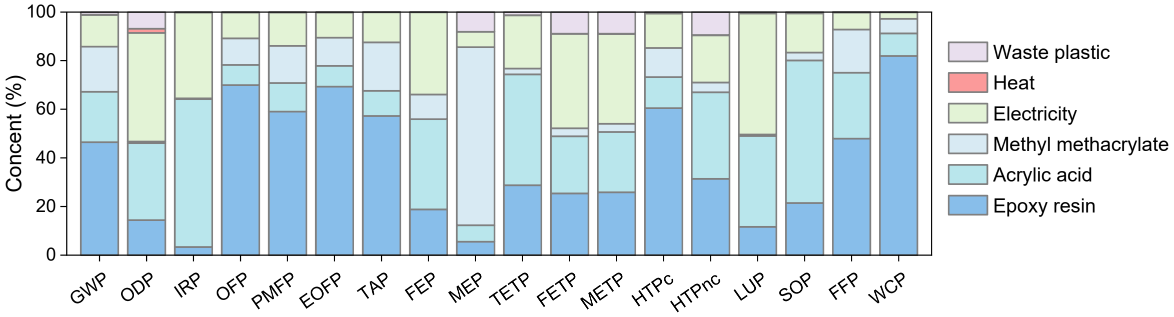

Supplementary Fig. 58. The impact on each indicator during the EAL30/Zn production process.

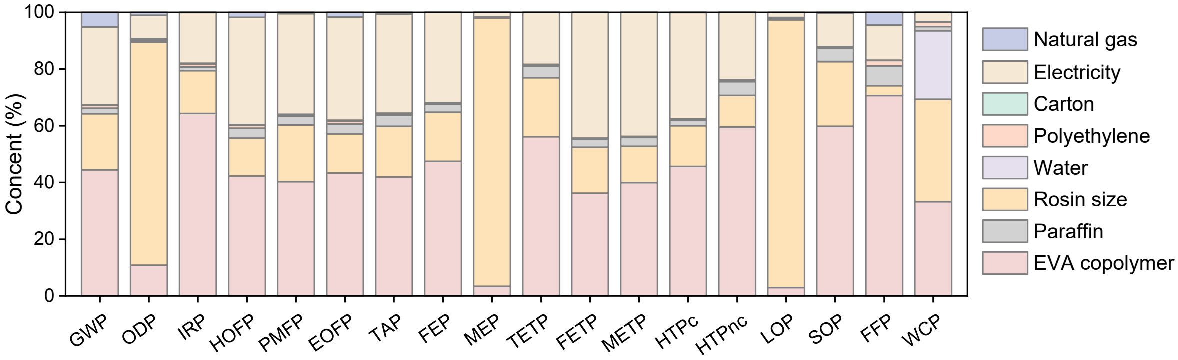

Supplementary Fig. 59. The impact on each indicator during the EVA production process.

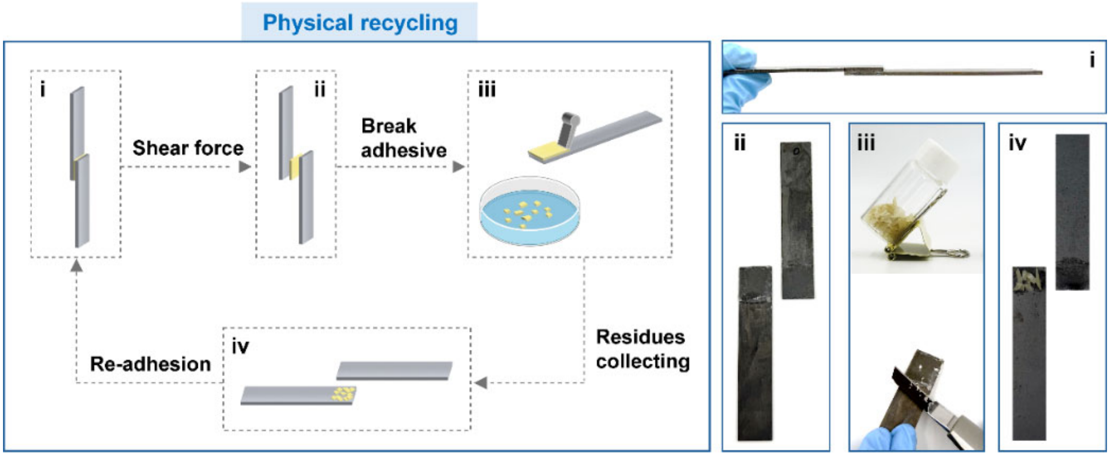

Supplementary Fig. 60. Closed-loop physical recycling and reuse performance of the adhesive system.

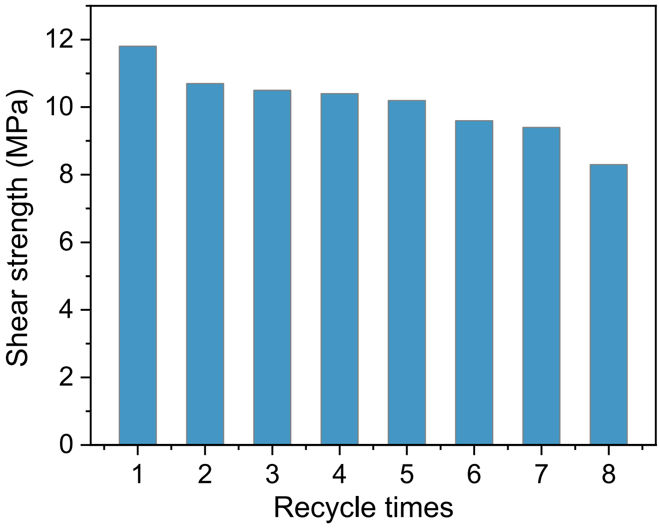

Supplementary Fig. 61. The shearing performance of 8 cycles of the cutting/recycling process.

Supplementary Table 1. Mechanical properties of photopolymers.

Sample	Stress (MPa)	Strain (%)	Fa (MPa)	Work of debonding (N m^{-1})
EAL	2.0	960.0	8.6	56519
EAL30	3.8	310.2	13.6	97642
EAL30/Zn	10.1	151.8	17.7	130983

References

(1) C. Wang, L. Luo, H. Yamamoto, Metal-catalyzed directed regio- and enantioselective ring-opening of epoxides. *Acc. Chem. Res.* 49, 193-204 (2016).

(2) Y. Wu et al., New acyl phosphine oxides as high-performance and low migration type I photoinitiators of radical polymerization. *Prog. Org. Coat.* 168, 106876 (2022).

(3) J. Chen et al., Effect of coordination sacrificial bond strength on toughening properties of polyesters. *Macromolecules* 57, 4054-4061 (2024).

(4) M. A. Gonzalez et al., Strong, tough, stretchable, and self-adhesive hydrogels from intrinsically unstructured proteins. *Adv. Mater.* 29, 1604743 (2017).

Supplementary videos

Supplementary Video S1. Tensile testing of EAL30/Zn.

Supplementary Video S2. Low-temperature testing of EAL.

Supplementary Video S3. Low-temperature testing of EAL30.

Supplementary Video S4. Low-temperature testing of EAL30/Zn.

Supplementary Video S5. Demonstration of adhesive load-bearing capacity (EAL30/Zn).

Supplementary Video S6. Substrate failure in bamboo (EAL30/Zn).

Supplementary Video S7. 3D XRM analysis of EAL (0.7um).

Supplementary Video S8. 3D XRM analysis of EAL30/Zn (0.7 um).